Doctoral Dissertation

Design, Preparation and Application of Noble Metal Catalysts in Biomass Conversion

(バイオマス変換における貴金属触媒の設計、調製と応用)

牛　文起
Wenqi Niu

Tsubaki Laboratory
Department of Applied Chemistry
Graduate School of Science and Engineering
University of Toyama, Japan
January, 2015

Preface

Recently, an increasing effort has been devoted to find ways to utilize biomass as feedstocks for the efficient production of value-added organic chemicals and fuels because of its abundance, renewability and worldwide distribution. Unlike petroleum feedstocks, biomass-derived platform molecules possess a high oxygen content that give them low volatility, high solubility in water, high reactivity and low thermal stability, as well as properties that favor the processing of these resources by catalytic aqueous-phase technologies at moderate temperatures. Lignocellulosic biomass encompassing municipal and animal wastes, forestry residues, and others is a special interesting resource on account of being the most abundant, inedible, and inexpensive biomass.

In this doctoral dissertation, biomass derived 5-hydroxymethylfurfural (HMF), cellulose and bio synthesis gas have emerged as important platform chemicals for the next-generation plastic and basic chemicals for the production of sustainable fuels and chemicals.

Furan derivatives such as 5-hydroxymethyl-2-furaldehyde (HMF) obtained from renewable biomass resource, has the potential to serve as substitutes for the petroleum-based building blocks that are currently used in the production of polymers and fine chemicals. In Section 1 (Chapter 1), reduced graphene oxide (RGO) is one of

the most promising catalyst supports since its faintly acidic sites together with large amount of functional groups on its surface. In this section, we prove that, for the first time, Pt loaded RGO (Pt/RGO) is an efficient, robust and durable catalyst oxidizing 5-hydroxymethylfufural (HMF) directly to 2,5-furandicarboxylic acid (FDCA) under mild conditions. The selectivity of FDCA reaches up to 84% along with 100% HMF conversion in the presence of excess base. We deduce that the total reaction on Pt/RGO catalyst includes several consecutive steps, in which 5-hydroxymethyl-2-furancarboxylic acid (HMFCA) acts as an intermediate. The finding in this report is a significant advance not only for RGO-based catalysts development, but also for FDCA scalable production, because the total reaction is performed smoothly without using previously reported harsh reaction conditions.

Furthermore, Cellulose, a polysaccharide mainly composed of glucose via β-1-4 glycosidic linkage, exists widely in biomass resources. The utilization of cellulose is achieved usually through two steps: being selectively hydrolyzed into glucose and further converted into fuels and chemicals. The sugar alcohols, especially sorbitol, are used not only as sweetener in diet foods, but also as an important basic chemical for the production of sustainable fuels and chemicals. In Section 2 (chapter 2-5), Pt nanocatalysts loaded on reduced graphene oxide (Pt/RGO) are prepared via a convenient microwave-assisted reduction approach with ethylene glycol as reductant. The conversion of cellulose or cellobiose into sorbitol is used as application reaction to investigate their catalytic performance. Various metal nanocatalysts loaded on RGO are compared. Pt/RGO exhibits the highest catalytic activity with 91.5% of sorbitol yield

from cellobiose. The catalytic performances are compared with Pt nanocatalysts supported on different carbon materials or on silica support. The result shows that RGO is the best catalyst support, and the yield of sorbitol is as high as 91.5% from cellobiose and 58.9% from cellulose, respectively. The improvement of catalytic activity is attributed to the appropriate Pt particle size and hydrogen spillover effect of Pt/RGO catalyst. Interestingly, the size and dispersion of supported Pt particle are easily regulated by convenient adjustment of the microwave heating temperature. The catalytic performance is found firstly increased and then decreased with increasing particle size. The optimum Pt particle size is 3.6 nm. These findings may offer useful guidelines to design novel catalysts with beneficial catalytic performance for biomass conversion.

Conversion of synthesis gas (a mixture of CO and H_2), derived from biomass, is a hot field in hydrocarbon production. Fischer-Tropsch synthesis is a set of catalytic processes that can be used to produce fuels and chemicals from synthesis gas. Combining a acidic zeolite with common FTS catalyst can produce isoparaffins for gasoline-ranged component. Tuning hydrocarbons distribution in Fischer-Tropsch synthesis is greatly challenging in Section 3 (chapter 6) by employing three different pathways to deposit trace Palladium on Co/H-ZSM5 catalyst, tunable isoparaffin and olefin selectivity is successfully achieved. The impregnated Pd shows a poor promotion of Co dispersion and reducibility, producing a slight enhancement of FTS activity and isoparaffin selectivity. Pd sputtering induces a re-dispersion of impregnated Co/H-ZSM5 particles and Pd is deposited with an intimate distance to Co species and with a weak interaction combining zeolite, due to which complete hydrogenation of olefins is achieved. But the surface enriched Pd on pre-sputtered Co catalyst was can

form Pd-Co nano-alloys, suppressing the chain growth activity by excessive hydrogenation process.

Content

Section I Efficient Conversion of HMF to FDCA

Chapter 1 Pt Nanoparticles Loaded on Reduced Graphene Oxide as an Effective Catalyst for the Direct Oxidation of 5-Hydroxymethylfurfural (HMF) to Produce 2,5-Furandicarboxylic Acid (FDCA) under Mild Conditions

1.1 Abstract:

Reduced graphene oxide (RGO) is one of the most promising catalyst supports since its faintly acidic sites together with large amount of functional groups on its surface. In this report, we prove that, for the first time, Pt loaded RGO (Pt/RGO) is an efficient, robust and durable catalyst oxidizing 5-hydroxymethylfufural (HMF) directly to 2,5-furandicarboxylic acid (FDCA) under mild conditions. The selectivity of FDCA reaches up to 84% along with 100% HMF conversion in the presence of excess base. We deduce that the total reaction on Pt/RGO catalyst includes several consecutive steps, in which 5-hydroxymethyl-2-furancarboxylic acid (HMFCA) acts as an intermediate. The finding in this report is a significant advance not only for RGO-based catalysts development, but also for FDCA scalable production, because the total reaction is performed smoothly without using previously reported harsh reaction conditions.

Keywords: HMF, FDCA, reduced graphene oxide, mild conditions, Pt nanoparticles

1.2 Introduction

Nowadays, 5-hydroxymethylfurfural (HMF), a biomass-derived intermediate, is readily available from a variety of renewable biomass resources such as fructose, glucose,[1] polysaccharides,[2] and cellulose.[3] 2,5-furandicarboxylic acid (FDCA) has been considered as a potential biorenewable monomer to replace terephthalic acid in the production of polyethylene terephthalate (PET).[4] Moreover, FDCA has also been identified as one of several important building blocks for the production of biomass-derived value-added chemicals.[5] Generally, the oxidation of HMF to FDCA can be catalyzed by various stoichiometric oxidants, such as $KMnO_4$,[6] or homogeneous metal salts (Co, Mn), those are currently used for terephthalic acid production under high pressure (70 bar air).[7] Different reaction systems using Pt-, Pd- or Ru-based heterogeneous catalysts have been reported for the selective oxidation of HMF to FDCA,[8,9] but these methods require high pressure or high temperature, and have lower catalyst stability and selectivity.

Recently, several reports have been presented using supported Pt catalysts for aqueous HMF oxidation to improve FDCA yields.[10-17] Using the supported Pt as catalysts, as reported by Davis et al.,[13] the addition of homogeneous base (1-20 eqiv. NaOH) and high oxygen pressure (3-20 bar) are required. Strasser et al. shows that the feedstock of HMF degrades rapidly at 353K in alkaline water.[15] In addition, Gupta et al. also reports a base-free oxidation in water over gold catalysts supported on hydrotalcites, yielding FDCA with almost 100% yield at 368K.[14] Although the Pt- and Au-based catalysts seem to be promising, the catalyst design and reaction conditions, especially reaction temperature and pressure must be further optimized.

Carbon material, such as activated carbon, had been reported as catalyst support in HMF oxidation reaction.[10,11,13,15-17] However, to our knowledge, graphene oxide, a novel carbon material, has not been reported as catalyst or support material in this reaction until now. Compared with other carbon materials, graphene oxide has attracted tremendous attentions in recent years due to its relatively stable physical properties and unique two-dimensional planar structure.[18] In addition, graphene oxide is slightly acidic since large amount of functional groups on its surface.[19,20] These functional groups on the surface of graphene oxide can be also utilized as anchoring sites fixing metallic nanoparticles, increasing the dispersion of the supported nanocatalysts and tuning their catalytic performance. Moreover, the graphene sheet has spillover effect under H_2 or O_2 reaction atmospheres especially when noble metal exists as supported catalyst.[21] These special performances may be beneficial for the oxidation of HMF when the Pt loaded reduced graphene oxide (Pt/RGO) is used as catalyst.

In this work, the Pt loaded graphene oxide (Pt/RGO) catalyst was prepared by ethylene glycol reduction method[22] and used in the HMF oxidation reaction to produce FDCA. Other metallic nanoparticles, like Pd, Ru, Rh and Pt, loaded on the reduced graphene oxide were also prepared and their catalytic performances were compared together. As the best catalyst for FDCA production, the Pt/RGO catalyst was investigated in detail. The possible reaction route on the Pt/RGO for HMF oxidation to form FDCA is presented in Figure 1.

1.3 Experimental Section

Hummer's method was used to prepare Graphite Oxide (GO).[23] 10.0 g graphite powder and 5.0g $NaNO_3$ were mixed in a flask, and cooled in ice bath. 230 ml of concentrated H_2SO_4 solution was added into the above mixture. After stirring for 10 min, $KMnO_4$ was gradually added, and the mixture was kept stirring in an ice bath for another 15 min. The mixture was then kept at 308K and stirred for 50 min until a thick paste was obtained. 460 ml of water was added into the above mixture, and the reaction temperature was gradually increased to 371K. The mixture was kept at 371K and stirred for another 30min. Finally, 1000 ml of deionized water and 3.0 ml of 30% H_2O_2 were slowly added to the mixture and stirred for 5 min. The obtained yellow dispersion was washed by deionized water for several times to remove residual salt, and the solid (GO) was then dried under vacuum for 3 days.

H_2PtCl_6 (aq.) (Pt wt% =4.578%, 0.56 ml) and graphite oxide (1.0 g) were dispersed in 120ml of ethylene glycol (EG) (aq, EG v% = 83.3%) with the assistance of ultrasonic. After being treated ultrasonically for 2 h, the mixture was put into an oil bath and kept at 408K for 15 h. The catalyst was obtained through a redox reaction, and the solid product was then collected by filtration and washed with deionized water and ethanol in sequence, before drying. The final metal loading amount was 5.0 wt%, and the obtained catalyst was defined as Pt/RGO. Other metals loaded RGO catalysts Pd/RGO, Rh/RGO and Ru/RGO were also prepared by same method using $Pd(NO_3)_2$, $Rh(NO_3)_3$, $Ru(NO_3)_3$ as metal sources. Furthermore, pure RGO, as a reference catalyst, was also prepared by this method, but without any metals addition. In order to prove the combined function of active metal Pt and support RGO, another general catalyst support, active carbon (AC), had also been selected to prepare a reference catalyst Pt/AC.

The Pt/RGO catalyst morphologies were characterized with high-resolution transmission election microscope (TEM, JEOL JEM-2100 UHR) operated at 200 kV. The catalyst crystal structure was confirmed by X-ray Diffraction (XRD) with a Rigaku D/max-2250 V diffractometer employing Cu Kα radiation (λ = 1.54 A; scanning rate: 0.02°/s). X-ray photoelectron spectroscopy (XPS) was conducted using ESCALAB 250Xi spectrometer equipped with a pre-reduction chamber. The position of the C1s peak (284.5 eV) was used to correct the XPS binding energies for all catalysts to erase possible charging effect.

HMF oxidation reaction was carried out in a three-neck-flask attached with a glass reflux condenser under oxygen flow (see Figure 2). In each experiment, the reactor was filled with 1.0 mmol of HMF and 5.0 mmol of NaOH in 10 ml of water. 0.1 g M/RGO (M=Pd, Rh, Ru or Pt) was added into the reactor and oxygen was introduced at a flow rate of 50 ml/min with stirring under atmosphere pressure. After reaction, the catalyst was filtered off before the high performance liquid chromatography (HPLC) measurement (Animex HPX-87H column from Bio-Rad Laboratories Co. Ltd, 0.5 ml/min flow rate, 10 nM H_2SO_4 solvent, 323K). The products were analyzed using a refractive index (RI) detector.

1.4 Result and discussion

The crystal structure of the best catalyst Pt/RGO was confirmed by XRD. We used XRD to confirm whether the crystal structure of the spent Pt/RGO was identical to that before reaction. In Figure 3, the strong diffraction peak for two samples can be assigned to RGO. The diffraction peaks at 2θ= 39.6°, 42.6° and 67.5° can be ascribed to the characteristic peak of Pt (111), (200), and (220) crystalline planes of Pt respectively, which possesses fcc structure. The diffraction peak of Pt (111) was used to estimate the

Pt particle size by Scherrer equation. The calculated average particle size of Pt on RGO sheet is 3.28 nm before the reaction, and 3.60 nm after the reaction, indicating the selected reaction conditions has no obvious effect on Pt nanoparticles size.

The morphologies of the Pt/RGO catalyst were also characterized by TEM. As shown by Figure 4(a,b), highly dispersed Pt nanoparticles with a uniform size of 3.28 nm loaded on RGO surface were obtained by heating H_2PtCl_6 and GO in the ethylene glycol aqueous solution. In Figure 4(c,d), the Pt nanoparticle size of Pt/RGO increased slightly to 3.60 nm after reaction for 24h. These TEM images confirmed that the highly dispersed Pt nanoparticles with uniform size had been successfully synthesized and well located on the RGO sheets through ethylene glycol reduction method.

X-ray photoelectron spectra (XPS) using ESCALAB 250Xi spectrometer equipped with a pre-reduction chamber was used to investigate the surface composition of Pt/RGO catalyst. As shown in Figure 5(a), Pt 4f spectra of Pt/RGO exhibited the expected doublets of Pt 4f 7/2 and Pt 4f 5/2, with Pt^0, Pt^{2+} and Pt^{4+} states. It is interesting to note that a respectable percentage of Pt remained still in its metallic state (Pt^0) in Pt/RGO after being used for even 3 times, which can be found in Figure 5(b). In addition, two different types of Pt cations could be assigned, suggesting that the oxygen linkages existed between Pt nanoparticles and RGO surface, and the oxide layers formed on the Pt nanoparticles surface.

Besides C-C sp^2 (284.2eV) and C-C sp^3 (285.7eV), C-O (286.4eV) and C=O (288.9eV) are also observed by XPS, proving that a lot of functional groups formed on Pt/RGO catalyst surface.

Using wavelength dispersive X-ray flourescence spectrometer, it is clarified that oxygen content decreased slightly after reaction, 53.2wt% to 52.1wt% for GO while 20.8wt% to 19.8wt% for 5% Pt/RGO, due to the co-existing NaOH base. This changing trend is in accordance to the reported findings [24-26], where high-concentration NaOH solution treatment lowered the oxygen content in GO.

Different kinds of metallic nanoparticle such as Pd, Rh, Ru, Pt loaded on RGO were also prepared and evaluated. All the catalysts were prepared by the same EG reduction method. As listed in Table 1, Pd/RGO and Pt/RGO catalysts demonstrated almost 100% conversion of HMF. Pt/RGO and Pd/RGO yielded FDCA, whereas Ru/RGO and Rh/RGO gave HMFCA as main product, along with some decomposition by-products such as levulinic acid and 2,5-bishydroxymethylfuran (BHMF). Pt/RGO catalyst resulted in the highest yield of FDCA about 41%. The order of FDCA yield is as follows: Pt/RGO>Pd/RGO. In addition, Pt supported on activated carbon (Pt/AC), as a reference catalyst, was prepared and tested under the same reaction condition. Pt/AC provided a poor HMF conversion together with lower FDCA selectivity than Pt/RGO.

The BET surface area of Pt/AC was 950 m^2g^{-1} and that of Pt/RGO was 327 m^2g^{-1}. Although the surface area of Pt/RGO catalyst was lower, its higher activity indicated that its Pt dispersion and its tuned Pt reduction degree, along with the electronic state provided by the special two-dimensional planar structure from RGO, determined highly efficient redox reaction happening on its surface. It is referred that very fine Pt particles on the activated carbon with large surface area are readily oxidized but difficult to be reduced, lowering the redox reaction efficiency.

As shown in Table 2, Pt/RGO and Pd/RGO catalysts were compared in a shorter time experiment, 30min. Both conversion and FDCA selectivity of Pt/RGO were higher than those of Pd/RGO.

Time course of product formation for HMF oxidation over Pt/RGO was shown in Figure 6. According to the reaction process, about 71% of HMF was converted in first 2 h, and it was completely converted in another 5 h. 5-hydroxymethyl-2-furancarboxylic acid (HMFCA) was obtained as a critical intermediate at the initial step of the reaction without any by-products. This tendency was in good agreement with previous study using Pt/C under different reaction conditions.[15] In the initial step of reaction, HMF was selectively converted into HMFCA, suggesting that CHO group reacted faster than CH_2OH group. The yield of FDCA increased with time by oxidizing both aldehyde and alcohol groups, and 84% yield of FDCA was obtained at reaction time of 24 h. To date, 5-formyl-2-furancarboxylic acid (FFCA), another oxidation product, has been observed by Gupta el et.[14] However, in our experiments, we could not find FFCA in product. We deduce that it was rapidly converted into FDCA through a possible reaction route as in Figure 7.

In order to study the stability of Pt/RGO catalyst, it was reused for 3 times, without obvious deactivation as in Figure 8. The catalyst was simply reused again after washing with water at room temperature followed by vacuum drying. HMF was completely converted for all cases, and the FDCA yield was generally stable but accompanied by slight decrease.

1.5 Conclusions

In summary, Pt/RGO catalyst was prepared by ethylene glycol reduction method. The Pt/RGO catalyst exhibited high activity and selectivity for the oxidation of 5-hydroxymethylfufural (HMF) to produce 2,5-furandicarboxylic acid (FDCA) in water solution at room temperature. 84% yield of FDCA was achieved by using this Pt/RGO as catalyst. HMFCA was observed as an only intermediate during reaction process. The Pt/RGO catalyst could be reused at least for three times without obvious deactivation.

Tables and Figures

Table 1. HMF oxidation in water using M/RGO as catalyst under mild conditions.

Entry	Catalyst	HMF Conv. (%)	FDCA Selec. (%)	Yield (%)		
				HMFCA	FDCA	By products
1	GO	17.2	0	15.3	0	2.0
2	RGO	79.8	0	50.7	0	29.1
3	5% Pd/RGO	100	30.5	69.5	30.5	0
4	5% Ru/RGO	47.2	0	28.5	0	18.7
5	5% Rh/RGO	35.4	0	24.2	0	11.1
6	5% Pt/RGO	100	40.6	59.4	40.6	0
7	5% Pt/AC	62.6	38.2	38.7	23.9	0

Reaction conditions: HMF (1 mmol), H_2O (10 ml), catalyst (0.1 g), NaOH (5 mmol), under O_2 flow (50 ml min^{-1}), 298 K, 6h. The metals loading amount for every metals supported catalyst was 5 wt%.

Table 2. Product distribution of HMF oxidation in short reaction time.

Catalyst	HMF Conv. (%)	FDCA Selec. (%)	Yield (%)		
			HMFCA	FDCA	Byproducts
5% Pt/RGO	19.2	23.2	14.7	4.5	0
5% Pd/RGO	13.8	15.4	11.6	2.1	0

Reaction conditions: HMF (1 mmol), H_2O (10 ml), catalyst (0.1 g), NaOH (5 mmol), under O_2 flow (50 ml min^{-1}), 298 K, 30min. The metals loading amount for every metals supported catalyst was 5 wt%.

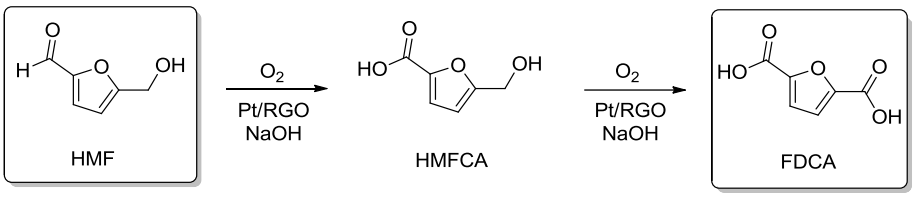

Figure 1. 2,5-Furandicarboxylic acid (FDCA) synthesis from oxidation of 5-hydroxymethylfurfural (HMF) catalyzed by Pt/RGO.

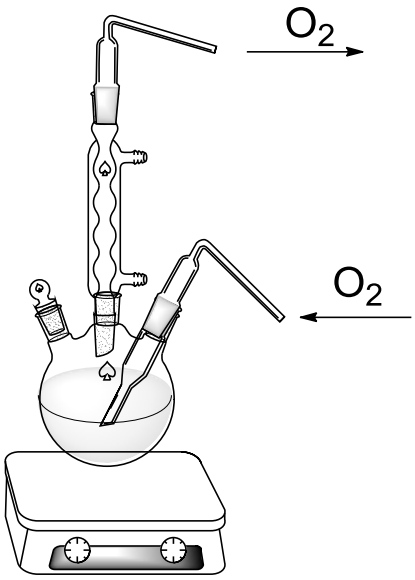

Figure 2. Reaction apparatus of HMF oxidation.

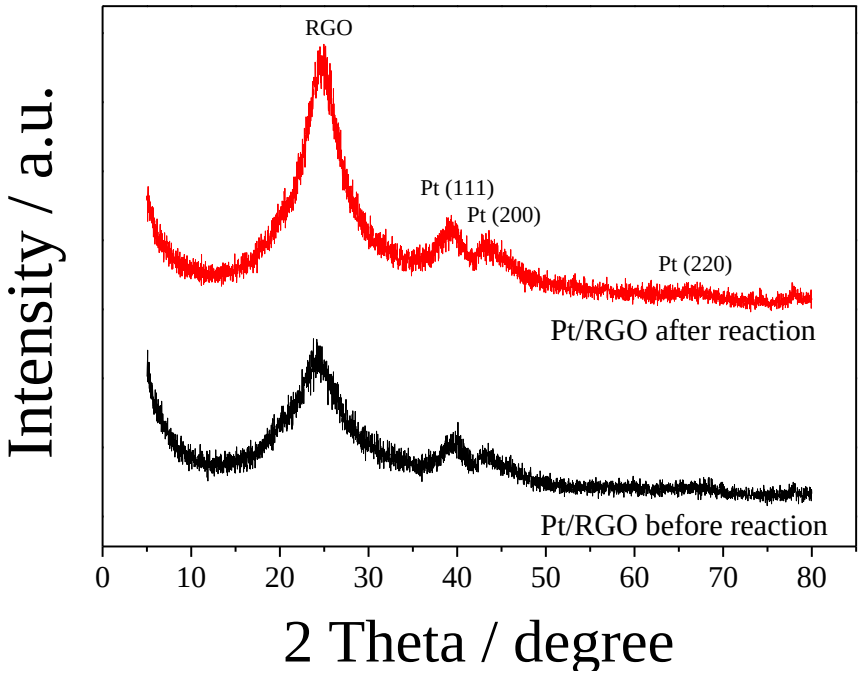

Figure 3. XRD patterns of Pt/RGO (before and after reaction).

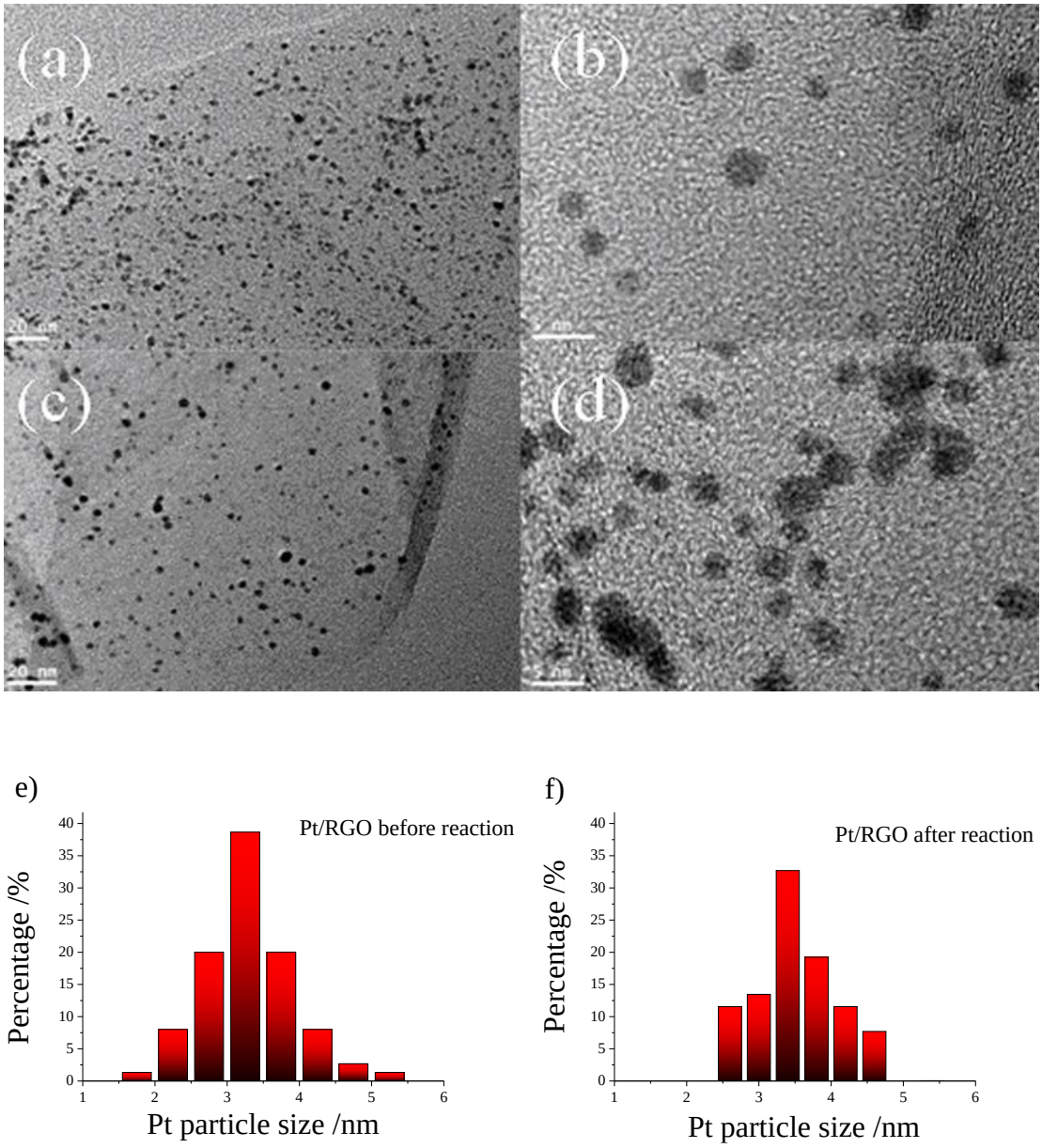

Figure 4. TEM images of Pt/RGO before reaction (a), (b) and after reaction (c), (d). The (e) and (f) give the Pt particles size distribution of two samples.

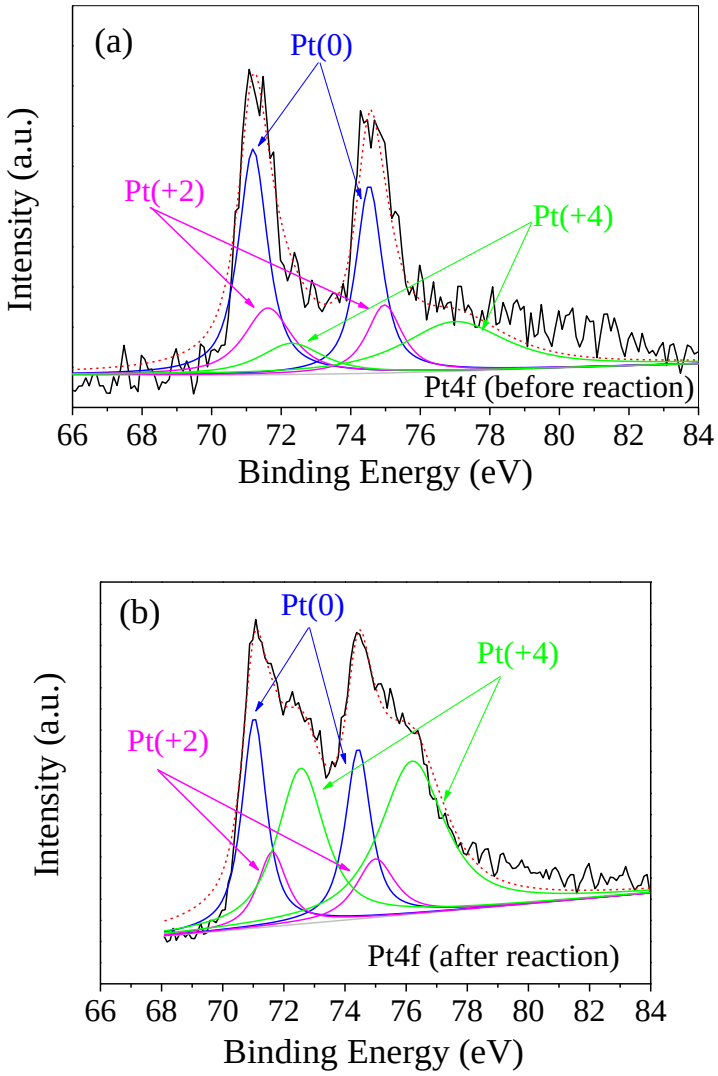

Figure 5. XPS spectra of Pt/RGO before (a) and after reaction (b).

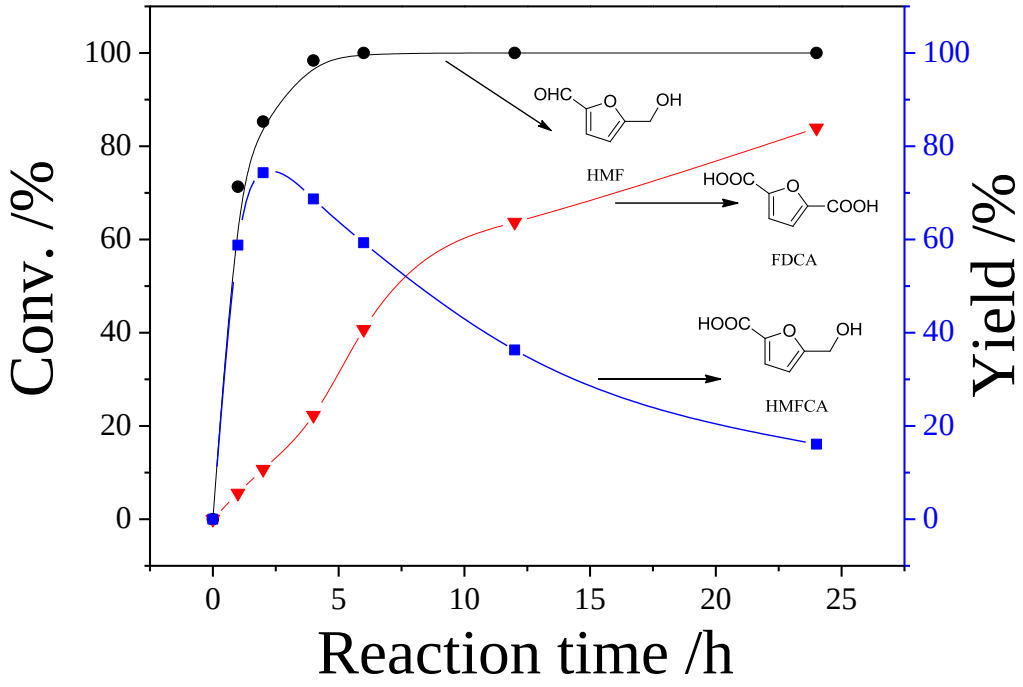

Figure 6. Time course of product distribution for HMF oxidation over Pt/RGO catalyst in water using atmospheric pressure of oxygen at 298 K. Reaction conditions: HMF (1 mmol), H_2O (10 ml), 5 wt% Pt/RGO (0.1 g), NaOH (5 mmol), under O_2 flow (50 ml min^{-1}), 298 K. HMF conversion (●), HMFCA yield (■), and FDCA yield (▼).

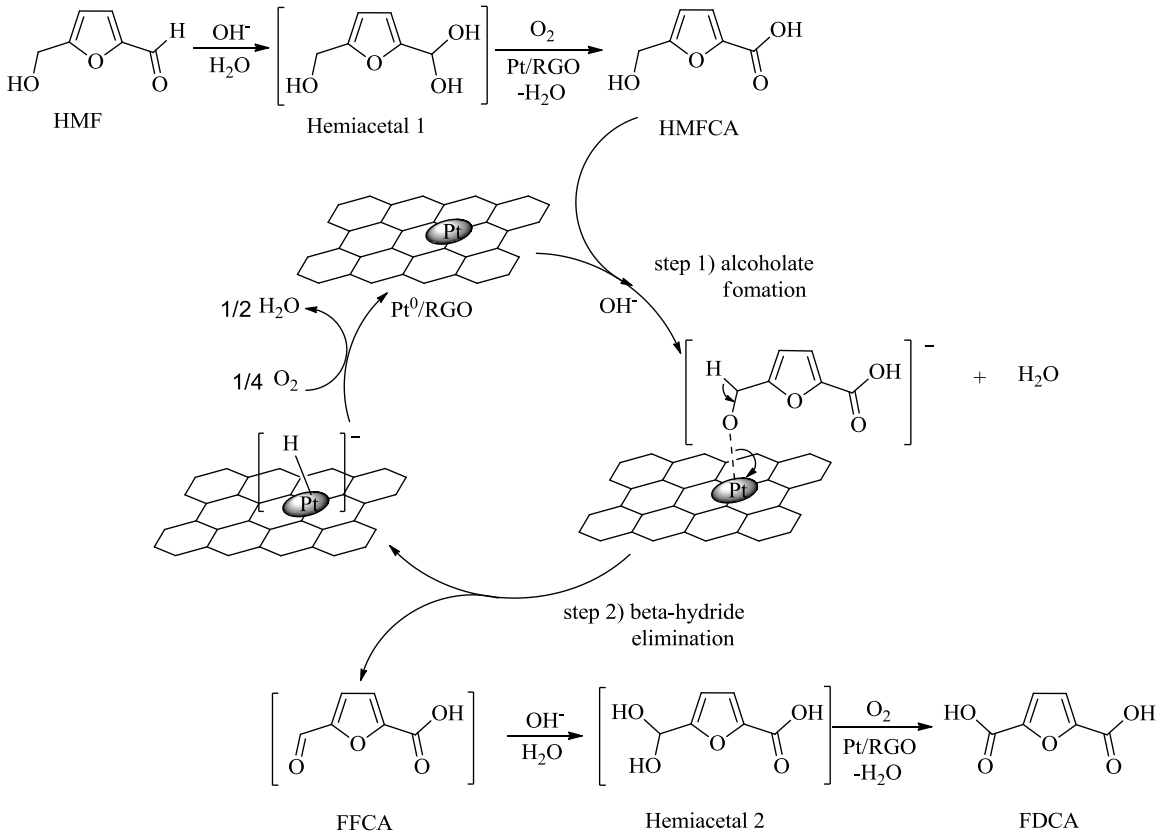

Figure 7. A proposed reaction route.

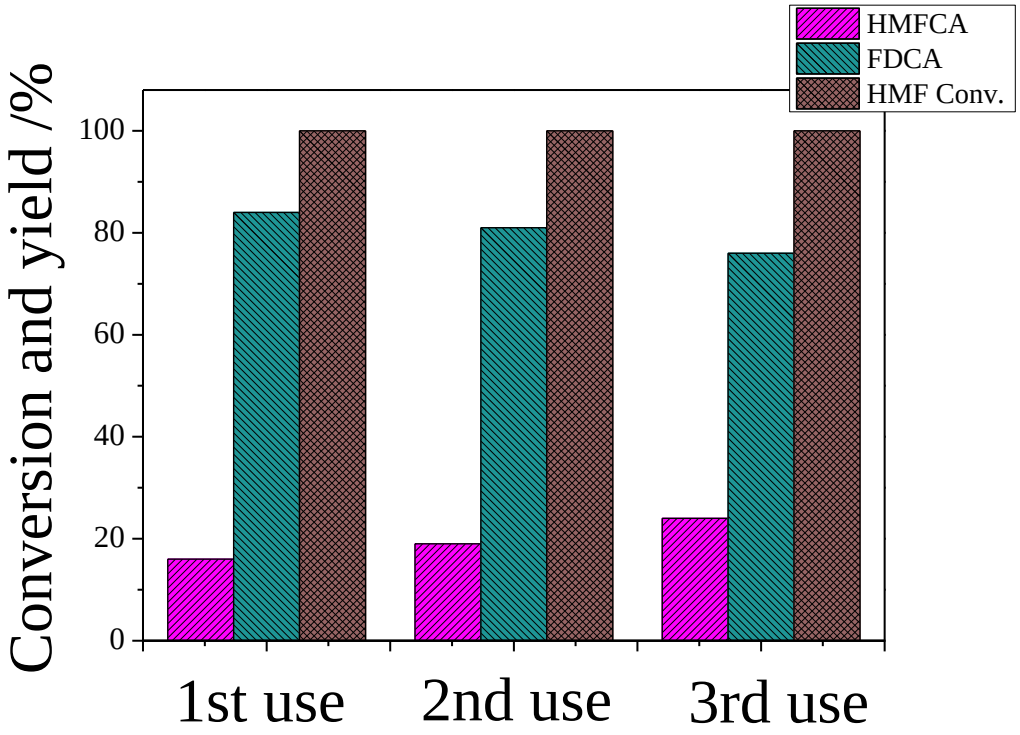

Figure 8. Recycling of Pt/RGO catalyst. *Reaction conditions*: HMF (1 mmol), H_2O (10 ml), 5 wt% Pt/RGO (0.1 g), NaOH (5 mmol), under O_2 flow (50 ml min^{-1}), 298 K, 24h.

Section II Highly Selective Conversion of Cellulose or Cellobiose to Sorbitol

Chapter 2 Introduction

Production of fuels or chemicals from the renewable biomass resources instead of fossil resources has attracted great attention in recent years.[27] Cellulose, a polysaccharide mainly composed of glucose via β-1-4 glycosidic linkage, exists widely in biomass resources.[28] The conversion of cellulose into fuels or industrial chemicals can avoid potential conflicts with the food supply, which has been regarded as a key issue on sustainable energy production.[29] The utilization of cellulose is achieved usually through two steps: being selectively hydrolyzed into glucose and further converted into fuels and chemicals.[30] Recently, the directly catalytic conversions of cellulose to sugar alcohol, ethylene glycol (EG) and gluconic acid have been reported.[31-33] The sugar alcohols, especially sorbitol, are used not only as sweetener in diet foods, but also as an important basic chemical for the production of sustainable fuels and chemicals.[34] Many catalysts, e.g. Pt/Al_2O_3, Ru/carbon nanotubes, Ru/activated carbon, Ni_xP, Pt/Na(H)-ZSM-5 have been used to convert cellulose or cellobiose into sorbitol directly.[31, 35-38] Nevertheless, few solid catalysts can obtain sorbitol with high yield when microcrystalline cellulose is used as feedstock except under harsh reaction conditions.[35-37]

In the conversion of cellulose to sorbitol, the catalyst used can accelerate hydrolysis or/and hydrogenation reactions (Scheme 1). Carbon material is a good choice as the catalyst support due to its excellent stability under hydrothermal conditions and large surface area for dispersed active components.[39] Carbon materials including activated carbon, mesoporous carbon and carbon nanotubes were reported as supports in cellulose conversion reaction.[31, 36, 39] However, to our best knowledge, graphene oxide, a novel carbon material, has not been reported as catalyst or as support material in cellulose conversion. Compared with other carbon materials, graphene oxide, one-atom thick

planar sheet of hexagonally arrayed sp^2 carbon atoms, has attracted tremendous attentions in recent years due to its relatively stable physical properties and its unique two-dimensional planar structure.[40] In addition, graphene oxide is slightly acidic due to large amount of surface functional groups. [41, 42] Carbon catalyst based on graphene oxide for facilitating oxidation and hydration reactions was reported. [43] In addition, these abundant functional groups on the surfaces of graphene oxide also can be utilized as anchoring sites for the loaded metal nanoparticles, which can increase the dispersion of the supported nanocatalysts and tune their catalytic performance. Furthermore, the graphene sheet has spillover effect under reaction atmospheres (such as H_2 and O_2) especially when noble metal exists as supported catalyst.[43] These unique performances may be beneficial for the cellulose conversion when graphene oxide or its derivative is used as catalyst support.

The preparation method of catalysts directly influences their catalytic performance due to intrinsic relationship between catalyst structure and their reactivity. The nanoparticles loaded on graphene oxide have been reportedly prepared by physical methods such as electrostatic attraction, photoreduction, electrophoretic or electrochemical deposition methods.[44-46] There were also prepared by chemical methods including hydrothermal/solvothermal method, ethylene glycol reduction, solid-state reaction method etc.[47-49] Normally, these methods are complicated and time-consuming. A rapid and convenient method to prepare metal nanoparticles supported on graphene oxide catalysts is expected.

In this section, the catalyst prepared by microwave assisted reduction method was used in the conversion of cellulose or cellobiose. Cellobiose, a glucose dimer connected

by a glycosidic bond, representing the simplest model molecule of cellulose, [50] was used in some experiments to investigate catalytic performance or reaction mechanism of catalyst. Here, the catalytic performances of carbon materials (activated carbon (AC), graphite oxide (GO), reduced graphene oxide (RGO), carbon nanotubes (CNTs) and graphene (G)) were firstly studied. Then, various metal nanoparticles loaded on RGO were prepared and their catalytic performances were compared. Furthermore, the influence of supports on catalytic performance was researched. As the best catalyst, Pt/RGO catalyst was investigated in detail. Finally, the reaction mechanism was explored.

Schemes

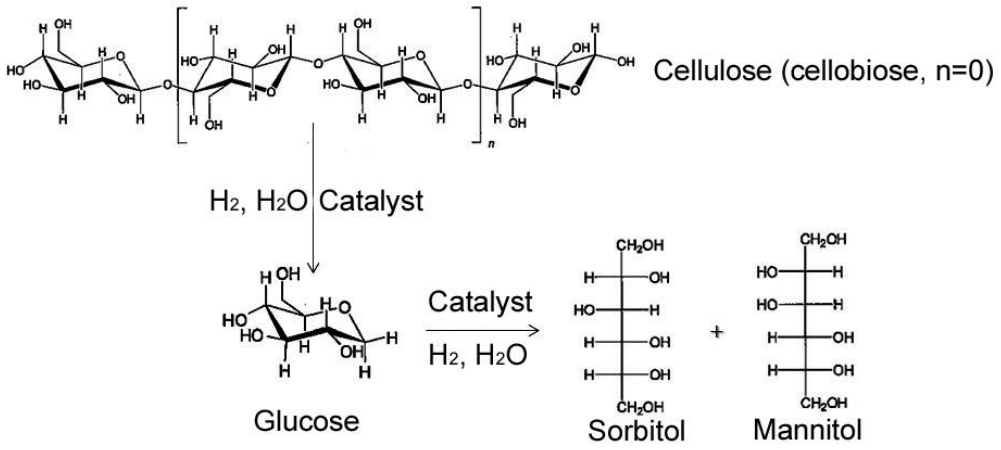

Scheme 1. Schematic representation for catalytic conversion of cellulose or cellobiose into sorbitol and mannitol.

Chapter 3 Catalytic performance of Carbon Materials and different metal nanocatalysts supported on RGO

3.1 Experimental

The carbon materials such as GO (preparation by modified Hummers method from expanded graphite),[51] AC (after acid treatment), SiO_2 (ID, after calcinated at 773K), G (prepared by thermal exfoliation of graphite oxide), [52] and CNTs (after acid treatment) [53] were chosen as catalysts to catalyze cellobiose to sugar alcohols.

Activated carbon (AC, Kanto Chemical Co.): AC with 20–40 meshes was refluxed with 35 % HNO_3 at 363 K for 6h, followed by washing with deionized water until pH = 7, and then dried over 12 h at 333 K.

Carbon nanotubes (CNTs, inner diameter: 4-10 nm; length, 0.5-2μm; Chengdu Organic Chemistry Co., Ltd.): the raw CNTs were refluxed with 65 % HNO_3 at 393 K for 14 h, followed by washing with deionized water until pH = 7, and then dried over 12 h at 333 K.

Graphite oxide (GO): 10.0 g graphite powder and 5.0 g $NaNO_3$ were mixed in a flask, and then cooled in ice bath. 230 mL concentrated (98 wt %) H_2SO_4 solution was then added to the mixture. After 10 min of stirring, $KMnO_4$ was added gradually and kept stirring in ice bath for another 15 min. The mixture was then kept at 308 K and stirred for 50 min until a thick paste formed. 460 mL deionized water was then added, and the reaction temperature was increased gradually. The mixture was kept at 371 K and stirred for 30 min. Finally, 1000 mL deionized water and 3 mL 30 % aq. H_2O_2 were slowly added to the mixture and stirred for 5 min. The obtained yellow dispersion was repeatedly washed with deionized water to remove remaining salt, and the obtained GO was then dried under vacuum at 323 K for 3 days.

Graphene (G): The obtained GO was placed inside a tubular furnace. The furnace was then heated to 523 K in Ar. High-purity H_2 gas was put in at that temperature, and G was obtained after 1-5min.

Reduced graphene oxide (RGO): RGO was prepared by the same method as Pt/RGO. The only difference was that Pt salt was not used in the preparation of RGO.

EG reduction with the assistance of microwave was applied to load metallic nanoparticles on RGO or on other support materials. Metal salt solution, such as H_2PtCl_6, $RuCl_3$, H_2PdCl_6, $Ni(NO_3)_2$ or $Cu(NO_3)_2$ solution, was chosen as metal source to prepare the metallic nanoparticles. For example, in a typical synthesis of Pt/RGO catalyst, the GO and H_2PtCl_6 were dispersed in EG solution with the assistance of ultrasonic. After being ultrasonically treated for 30 min, the mixture was then put into an automated focused microwave system and treated at 393-453 K for 30 min. The catalysts were obtained through a redox reaction heated by microwave. The reduction reaction could be observed by a color change from yellow GO in the mixture of EG and aqueous solution, to dark black after 30 min of microwave heating. The solid products were then collected by filtration and washed with deionized water as well as ethanol being dried. The metal loading in all catalysts was 5 wt%.

3.2 Results and discussion

3.2.1 Catalytic performance of carbon materials

XRD in Figure 1 can track the interlayer variations and the crystalline properties of graphite, GO, G and RGO. Graphite shows a very sharp diffraction peak at 2θ= 26.26°, corresponding to the interlayer spacing of 0.34 nm. The diffraction peak (2θ) around 11.6° belongs to the reflection of GO, and the interlayer spacing (0.80 nm) is much larger than that of pristine graphite owing to the introduction of oxygen-containing functional groups such as hydroxyl, epoxy, and carboxyl groups on the surface of graphite sheet.[54] After reduction with the mixture of EG and water, the intensity of typical diffraction peak (11.6°) of GO decreases and the position of the peak shifts to a higher angle, which is ascribed to the partial reduction of GO and the exfoliation of the layered GO nanosheets. The G prepared with thermal exfoliation of GO do not show any sharp peaks, demonstrating disorder and exfoliation. However, a broad and weak peak at 25.3° appears to show some amount of reclustering.[55]

Figure 2 shows the reaction results of cellobiose conversion over various carbon materials. Without catalyst, cellobiose can be hydrolyzed with 89.2 % of total conversion and 32.7% of glucose selectivity. The hydrolysis process in the conversion of cellobiose to glucose can be carried out even in the absence of catalyst, which may be due to H_3O^+ formed by water auto-protolysis with the temperature increase. These observations are in agreement with a recent investigation of cellulose hydrothermal degradation.[56] The high conversion of cellobiose may be due to its simple molecular structure with a glucose dimer connected by a glycosidic bond. When carbon materials are employed as catalysts in the conversion of cellobiose, the conversion values are similar, but the product distribution is depended on different carbon catalysts. In Figure

2 and Table1, the by-products include 5-HMF, low molecular polyols, etc. For AC and G catalysts, the primary by-product is 5-HMF, which is consistent with a previous study in which the chemistry for the decomposition pathways of cellulose and glucose in water indicates that glucose undergoes isomerization to form fructose, which can then undergo dehydration to form HMF.[57] For CNTs, GO and RGO catalysts, the yield of HMF is decreased while the yields of hexitol and low molecular polyols including xylitol, erythritol, glycerol, and ethylene glycol are increased. For GO or RGO catalyst, the increased sorbitol yield may be due to the oxygen-containing functionalities (alcohols, epoxides, and carboxylates), their unique structure and the defect on graphene sheets.[58] The GO/RGO catalysts for acid catalysis or hydrogenation were also reported on epoxides ring opening by GO and nitrobenzene hydrogenation with the help of RGO, respectively.[59,60]

3.2.2 Catalytic performance of different metal nanocatalysts supported on RGO

The typical hydrogenation catalysts such as Ni, Cu, Pd, Rh, Ru and Pt loaded on RGO were prepared to improve the cellobiose conversion and the yield of sorbitol. All the catalysts were prepared by the same EG reduction method with the assistance of microwave (see Scheme 1). The advantage of microwave heating over other conventional heating methods is uniform and rapid, which dramatically reduces processing time, increases product yield, and enhances product purity and properties.[61] Furthermore, the employment of microwave as heat source has been demonstrated to provide unique effects such as “superheating” of solvents above their boiling point and the selective heating of strongly microwave-absorbing materials, which can increase the metal loading efficiency.[62] As shown in Figure 3, all the catalysts demonstrate almost

100 % conversion of cellobiose. The different product distributions are influenced by the synergistic effect between the loaded metal and RGO.

3.3 Conclusion

The catalytic performance of RGO is similar to that of GO, which indicates that the catalytic activity is not influenced by the GO reduction process. However, the yield of sorbitol on GO or RGO is also lower. Ni, Cu, Pd, Rh, Ru and Pt loaded on RGO were prepared to improve the cellobiose conversion and the yield of sorbitol. The order of sorbitol yield is as follows: Pt/ RGO >Ru/ RGO >Rh/ RGO >Ni/ RGO >Pd/ RGO >Cu/ RGO. The highest sorbitol yield together with no glucose producing is obtained for Pt/RGO, which indicates that Pt is the most suitable catalyst with the highest sorbitol yield approximately 91.5 %.

Tables and figures

Table 1. Catalytic conversions of cellobiose into sorbitol with carbon materials as catalyst.

Table 1. Catalytic conversions of cellobiose into sorbitol with carbon materials as catalyst.

Catalysts	Cellobiose conv/%	Yield of products/%					
		Glucose	Mannitol	Sorbitol	HMF	C2-C5 polyols[a]	Others[b]
Blank	89.2	32.6	0.8	1.0	24.3	N.d.	30.5
AC	95.5	27.4	3.1	2.7	10.5	2.3	49.5
CNTs	92.4	3.6	3.8	16.6	3.5	5.3	59.6
G	92.2	18.2	0.6	0.9	20.6	2.1	49.8
GO	97.4	3.0	3.9	16.5	1.2	14.5	58.3
RGO	94.7	2.2	3.9	18.5	2.3	12.7	55.1

[a]C2-C5 polyols: xylitol, erythritol, glycerol, ethylene glycol, [b]The others are the by-products which cannot be identified by HPLC analysis. (Reaction conditions: Catalysts weight =0.050 g; Cellobiose weight =0.171 g; Reaction time= 3 h; Temperature=463 K; Pressure=5 MPa; H_2 as reaction gas.)

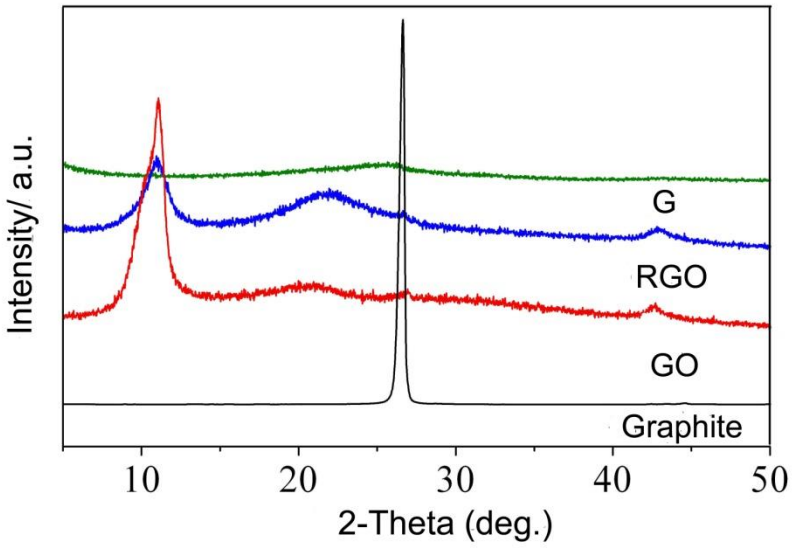

Figure 1. XRD patterns of graphite, graphite oxide (GO), reduced graphene oxide (RGO) and graphene (G)

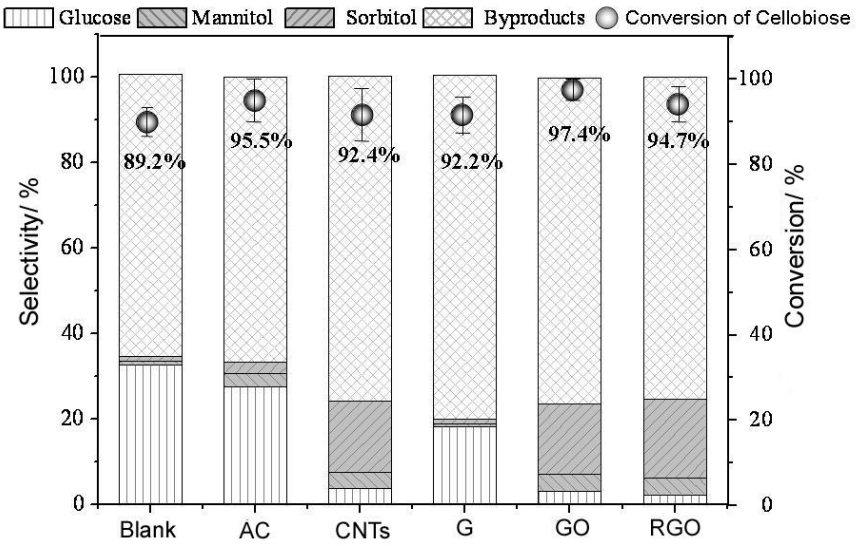

Figure 2. Catalytic conversions of cellobiose into sorbitol with carbon materials as catalyst. (Reaction conditions: Catalysts weight =0.050 g; Cellobiose weight =0.171 g; Reaction time= 3 h; Temperature=463 K; Pressure=5 MPa; H_2 as reaction gas.)

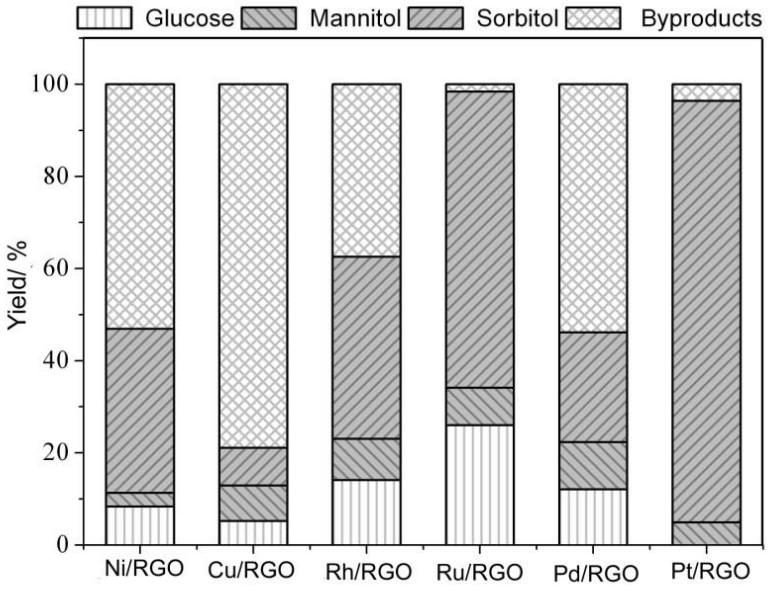

Figure 3. Catalytic performance of different metal catalyst (10 wt% Ni, 10 wt% Cu, 5 wt% Rh, 5 wt% Ru, 5 wt% Pd, 5 wt% Pt) supported on RGO catalyst for cellobiose conversion to sorbitol. (Reaction conditions: Catalyst weight =0.050 g; Cellobiose weight =0.171 g; Reaction time= 3 h; Temperature=463 K; Pressure=5 MPa; H_2 as reaction gas.)

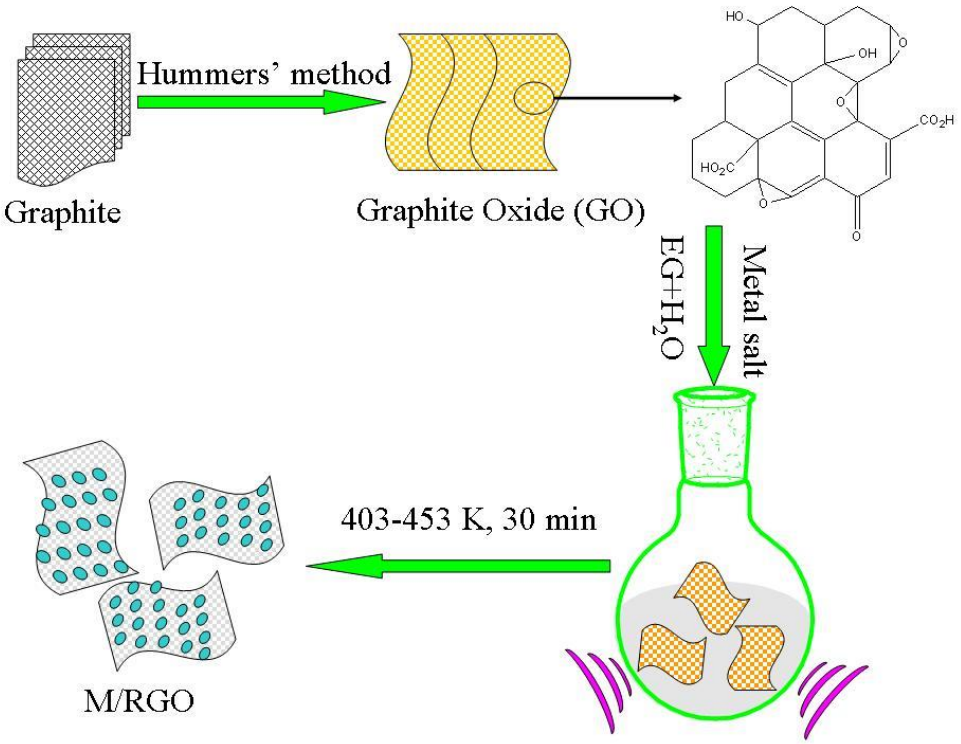

Scheme 1. Preparation schematic of M/RGO nanocatalysts with the assistance of microwave.

Chapter 4 Pt Nanocatalysts on Different Supports and Pt Particle Size Effect

4.1 Experimental

EG reduction with the assistance of microwave was applied to load metallic nanoparticles on RGO or on other support materials. Metal salt solution, such as H_2PtCl_6, $RuCl_3$, H_2PdCl_6, $Ni(NO_3)_2$ or $Cu(NO_3)_2$ solution, was chosen as metal source to prepare the metallic nanoparticles. For example, in a typical synthesis of Pt/RGO catalyst, the GO and H_2PtCl_6 were dispersed in EG solution with the assistance of ultrasonic. After being ultrasonically treated for 30 min, the mixture was then put into an automated focused microwave system and treated at 393-453 K for 30 min. The catalysts were obtained through a redox reaction heated by microwave. The reduction reaction could be observed by a color change from yellow GO in the mixture of EG and aqueous solution, to dark black after 30 min of microwave heating. The solid products were then collected by filtration and washed with deionized water as well as ethanol being dried. The metal loading in all catalysts was 5 wt%. The obtained catalyst was defined as M/RGO. RGO was prepared by the same method as above, but without the addition of metal salt. Pure Pt nanoparticles were prepared from the same EG reduction method without the existence of supports.

4.2 Results and discussion

4.2.1 Catalytic performance of Pt nanocatalysts on different supports

In order to clarify the functions of different supports on the conversion of cellobiose to sorbitol, Pt, the best active metal as above-mentioned, is also loaded on other supports. We used TGA to determine the Pt loading amounts on various carbon catalysts but there were no significant change, which means that the catalytic activity of Pt loaded on different carbon supports is comparable. As shown in Figure 1, the cellobiose conversion is as high as 100 %. The yield to sorbitol is just 41.9 % when Pt

nanoparticles is used as catalyst. Compared with Pt nanoparticles prepared by the same method, the yield of sorbitol is improved from 41.9 % to 91.5 % when RGO is used as Pt support. It is noted that not all support materials could improve the catalytic performance. From Figure 1, it is clear that with the same amount of Pt loaded, the catalytic activities have the following sequence: Pt/ RGO >Pt/ CNT >Pt nanoparticles> Pt/ AC >Pt/ SiO_2 >Pt/ G.

The XRD patterns of Pt nanoparticles loaded on different supports are displayed in Figure 2. The strong diffraction peaks at 2θ = 39.6°, 46.2° and 67.5° can be assigned to the characteristic (111), (200) and (220) crystalline planes of Pt. The average crystallite sizes were calculated by the Scherrer equation at 39.6°, which is showed in Table 1. Moreover, the morphology of Pt nanoparticles and Pt nanoparticles loaded on different supports was investigated by TEM. As in Figure 3, the dispersion and particle sizes of Pt are depended on supports. The particle size distribution in Figure 3 and Table 1 shows that the average size of Pt nanoparticles is about 3.5 nm for Pt nanoparticles, 3.6 nm for Pt/AC, 3.1 nm for Pt/CNTs, 1.2 nm for Pt/G, 3.6 nm for Pt/RGO and 3.1 nm for Pt/SiO_2. The Pt exposed surface area and dispersion were determined by chemisorption of CO. As in Table 1, the Pt exposed surface area and dispersion of catalyst also depend on supports. The Pt exposed surface area and dispersion are in the following sequence: Pt/RGO >Pt/SiO_2 >Pt/AC >Pt/CNTs >Pt/G. The catalyst with larger Pt exposed surface area and high dispersion usually has higher conversion in hydrogenation reaction.[63,64] Normally, the metallic catalyst with small metal particle size possesses high dispersion and high catalytic activity. Why the Pt dispersion of Pt/G and the catalytic activity of Pt/G are so low? The low catalytic activity of Pt/G catalyst may be due to the high oxidation states of metal catalyst on G support. As shown in Figure 4, Pt 4f spectra of

Pt/G show that the main valences of Pt are Pt^{2+} and Pt^{4+}. However, the Pt^0 is the active site in the cellobiose conversion reaction. The oxidation state of Pt can be attributed to the re-oxidation of oxygen in air. The high oxidation state may be also the reason that the Pt dispersion on Pt/G catalyst is so low. Compared with Pt/AC, the Pt/CNTs catalyst with similar Pt dispersion has better catalytic performance, which may be due to the following reasons: Firstly, most pores in AC are micropores, which is too small for cellobiose to enter.[63, 65] Secondly, CNTs with lots of surface functional groups formed by acid pretreatment have high sorbitol yield and low glucose yield, indicating that the CNTs have higher catalytic activity than AC in this reaction. With high Pt dispersion, Pt/SiO_2 has the lowest catalytic performance and this may be due to the same reason as Pt/AC. Therefore, the high catalytic activity is attributed to the synergistic effects of supports and the supported Pt nanoparticles. As in Figure 1, Pt loaded on RGO shows the highest catalytic performance, which indicates that RGO is the best support for the conversion of cellobiose to sorbitol.

4.2.2 The effect of Pt particle size on the catalytic performance

To disclose the effect of Pt particle size on the catalytic activity, Pt/RGO catalysts with different Pt particle sizes were prepared through the same reduction method. In this microwave assistant method, Pt particle size can be controlled with different temperature treatments. The XRD patterns of GO and Pt/RGO after different heat treatments are shown in Figure 5. It can be seen that the typical diffraction peak (002) of GO at 11.6° shifts to higher angle after the loading of Pt nanoparticles on RGO when the treatment temperature above 403 K, which indicates that the GO is converted to RGO. The strong diffraction peaks at 2θ = 39.6°, 46.2° and 67.5° can be assigned to the

characteristic (111), (200) and (220) crystalline planes of Pt, respectively, which possesses face-centered-cubic (fcc) structure. The diffraction peak of Pt (111) is used to estimate the Pt particle size by the Scherrer equation. The calculated average particle sizes of Pt on GO sheets are 2.0 nm for Pt/RGO-403 K, 2.7 nm for Pt/RGO-413 K, 3.6 nm for Pt/RGO-433 K and 4.3 nm for Pt/RGO-453 K, respectively.

Figure 6 shows the TEM images and Pt particle size distributions of Pt/RGO-T. All TEM images demonstrate that graphene nanosheets are uniformly decorated by distributed Pt nanoparticles with few aggregations, indicating a strong interaction between graphene support and Pt particles. The mean size of Pt nanoparticles is very consistent with the value estimated by Scherrer equation from Figure 5.

As in Figure 7, the yield of sorbitol increases with the mean size of Pt up to 3.6 nm and then decreases with further increasing Pt particle size. The highest catalytic performance is obtained by Pt/RGO-433 catalyst with 91.5 % of sorbitol yield. The similar trend is also observed when the cellobiose is replaced by cellulose. The highest yield of hexitol is 69 % (58.9 % of sorbitol and 10.1 % of mannitol). The results show that the Pt particle size is one of the critical factors affecting on the cellulose conversion. In addition, the catalytic activity may also be affected by the RGO supports processed at different microwave temperatures.

4.3 Conclusion

Pt loaded on RGO shows the highest catalytic performance, which indicates that RGO is the best support for the conversion of cellobiose to sorbitol. Pt particle size is one of the critical factors affecting on the cellulose conversion.

Tables and Figures

Table 1. The physicochemical properties of different catalysts.

Catalyst	Exposed Pt surface area [a] [m^2/g]	Pt Dispersion [a] [%]	Particle size by TEM [b] [nm]	Crystallite sizes by XRD [c] [nm]
Pt/SiO_2	65.2	26.4	3.1	2.9
Pt/AC	33.9	13.7	3.6	7.7
Pt/CNTs	31.6	12.8	3.1	4.0
Pt/G	8.7	3.5	1.2	-[d]
Pt/RGO	79.2	32.3	3.6	3.6

[a] The surface area was determined by CO chemisorption. [b] The average size of nanoparticles was evaluated from counting and averaging TEM images. [c] The average crystallite sizes were calculated by the Scherrer equation at 39.6°. [d] The diffraction peak was too low to estimate.

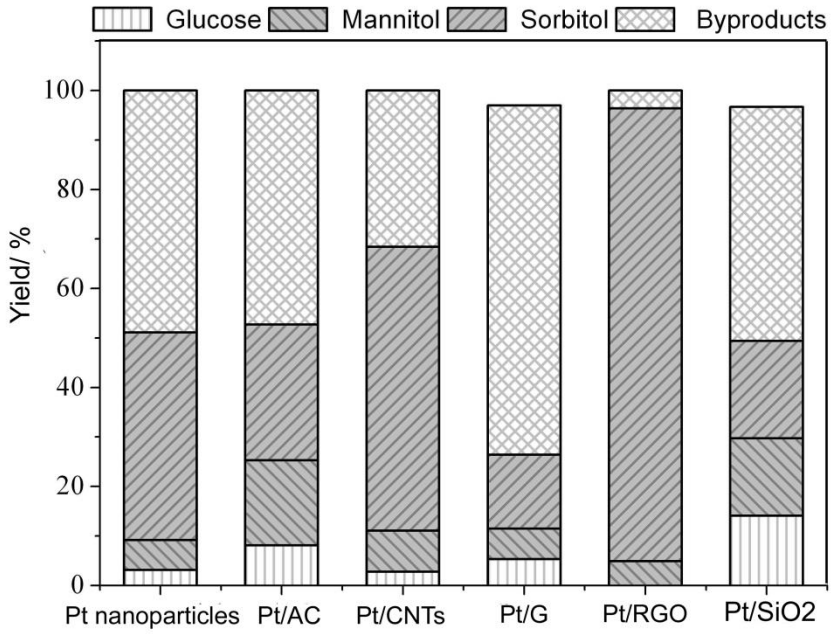

Figure 1. Catalytic performance of Pt loaded on different supports for cellobiose conversion to sorbitol. (Reaction conditions: Catalyst weight =0.050 g (Pt nanoparticles, 0.0025g); Cellobiose weight =0.171 g; Reaction time= 3 h; Temperature=463 K; Pressure=5 MPa; H_2 as reaction gas.)

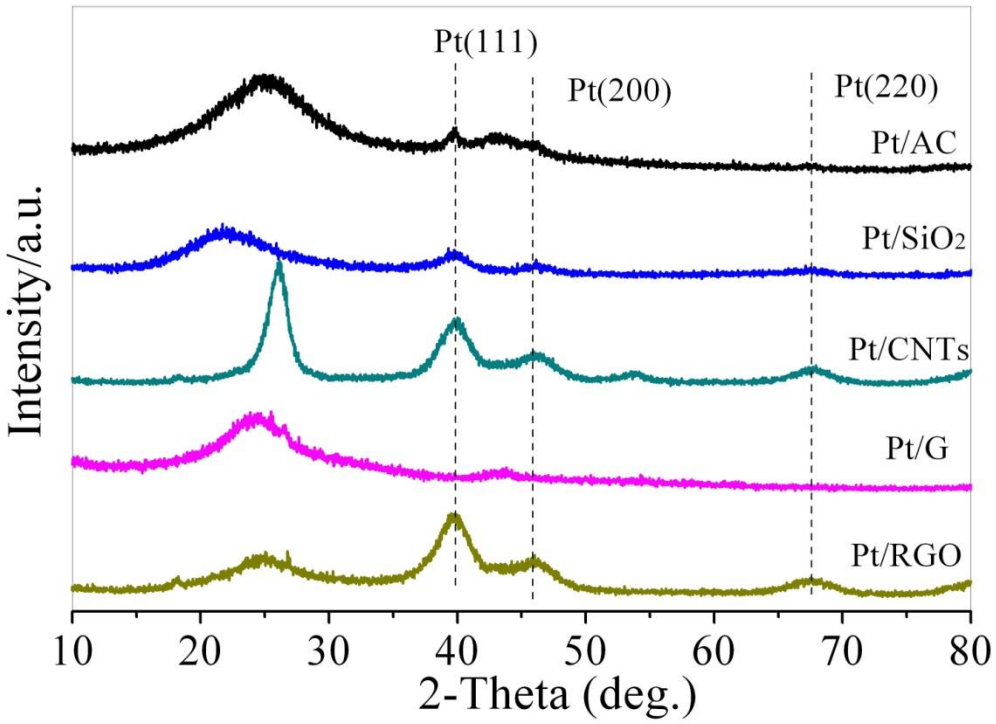

Figure 2. XRD patterns of Pt loaded on different supports (AC, SiO_2, CNTs, G, RGO).

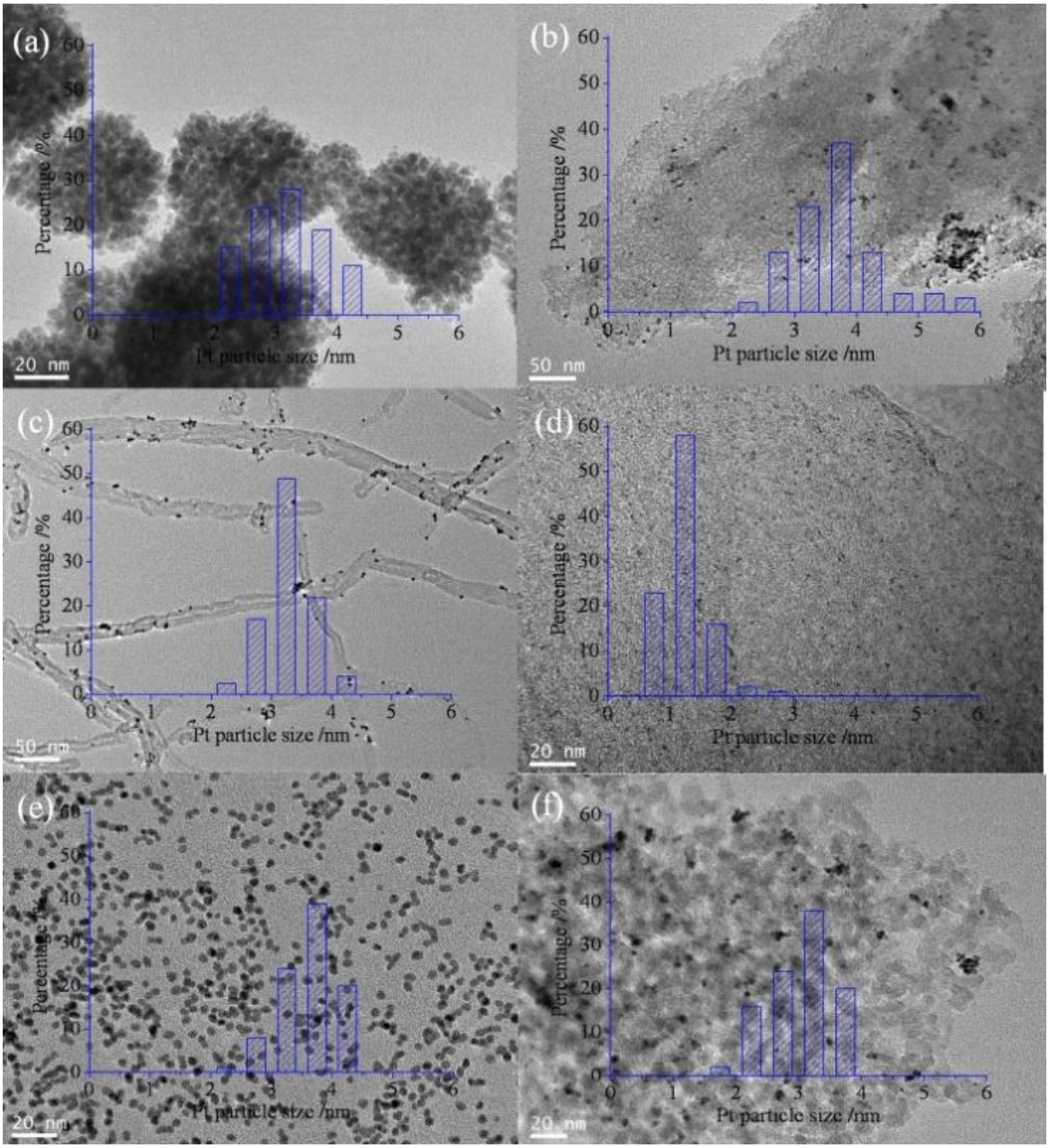

Figure 3. TEM images of (a) Pt nanoparticles and Pt nanoparticles loaded on (b) AC, (c) CNTs, (d) G, (e) RGO and (f) SiO_2.

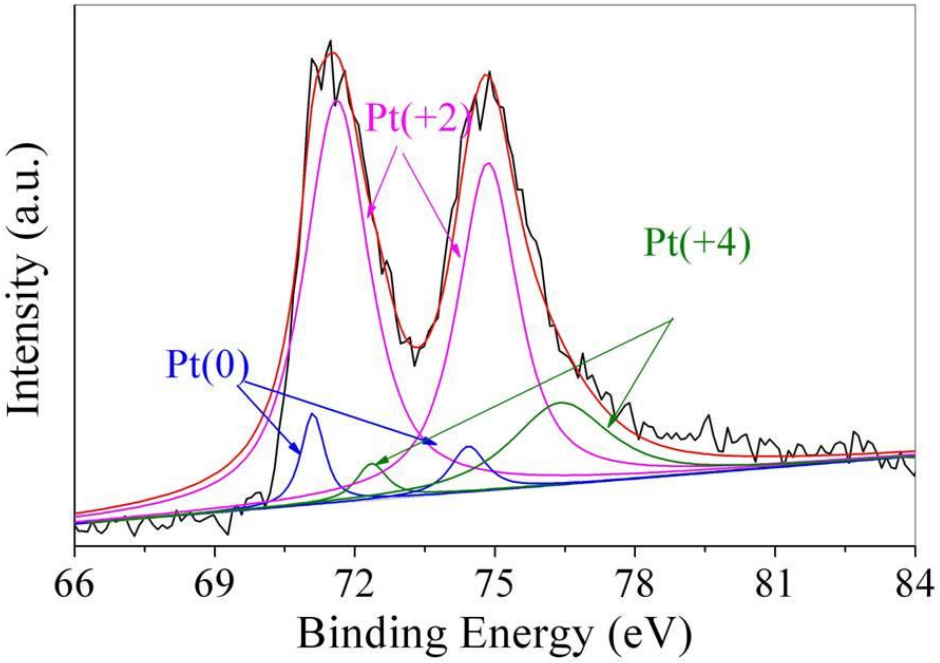

Figure 4. The XPS spectra of the Pt/G catalyst (Pt 4f region of Pt/G).

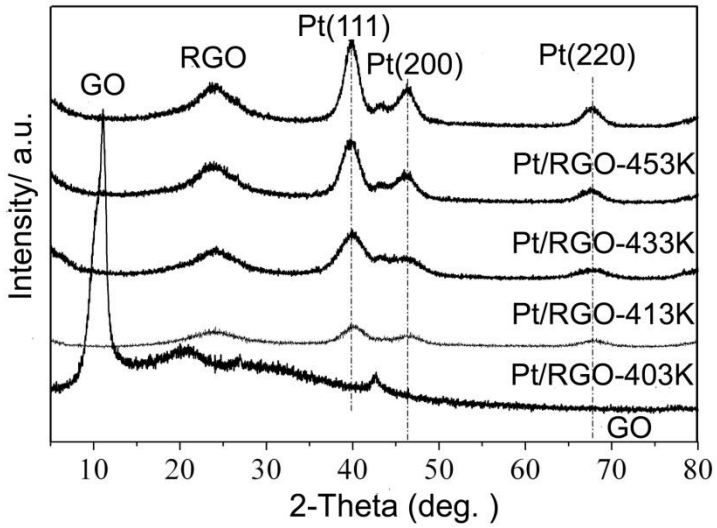

Figure 5. XRD patterns of GO and Pt/RGO-T (T=403 K, 413 K, 433 K, 453 K).

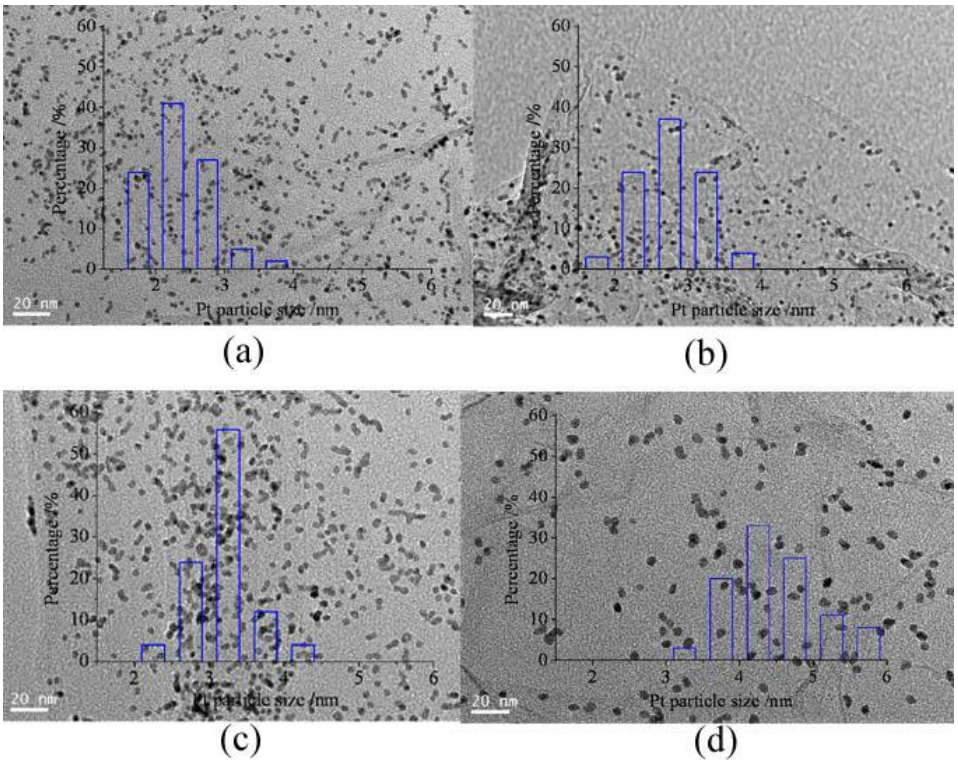

Figure 6. TEM images and particle size distribution of Pt/RGO-T (T=403 K (a), 413 K (b), 433 K (c) and 453 K (d)).

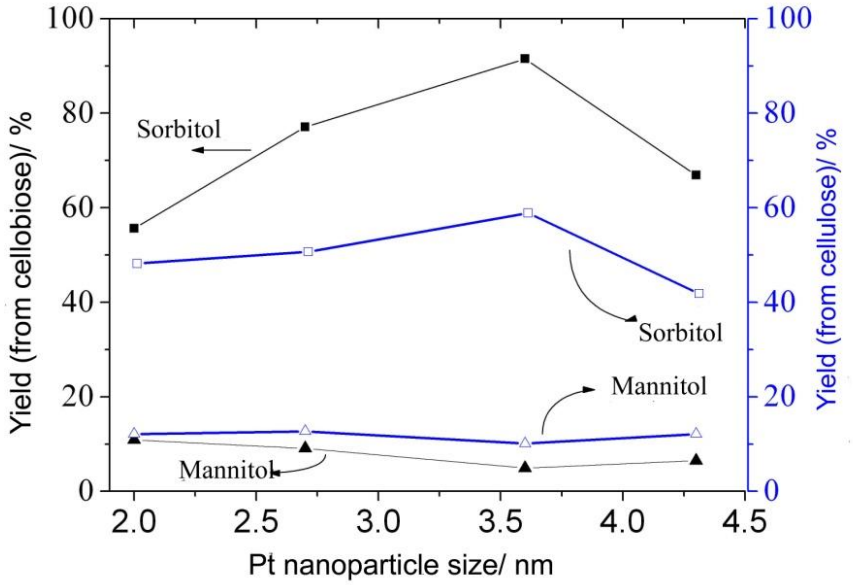

Figure 7. Conversions of cellobiose and cellulose into sorbitol and mannitol by Pt/RGO-T catalysts with different particle size (T=403 K, 413 K, 433K and 453 K). (Reaction conditions: Catalyst weight =0.050 g; Cellulose or cellobiose weight =0.171 g; Reaction time=24 h for cellulose and 3 h for cellobiose; Temperature=463 K; Pressure=5 MPa; H_2 as reaction gas.)

Chapter 5 Pt/RGO Catalyst and Reaction Mechanism of Cellulose Conversion

5.1 Experimental

5.1.1 Characterization of catalysts

The morphologies of the samples were characterized with high resolution transmission electron microscope (TEM, JEOL JEM-2100 UHR) operated at 200 kV. The crystal structure of the materials was confirmed by X-ray Diffraction (XRD) with a Rigaku D/max-2550 V diffractometer employing Cu Kα radiation (λ = 1.54 Å; scanning rate: 0.02 °/s). X-ray photoelectron spectroscopy (XPS) was conducted using ESCALAB 250Xi spectrometer equipped with a pre-reduction chamber. The position of the C1s peak (284.5 eV) was used to correct the XPS binding energies for all catalysts for possible charging effects. Thermal analysis was carried out on a DTG-60 (Shimadzu) in air flow. The loading amount of Pt was checked through inductive coupled plasma emission spectrometer (Shimadzu ICPE-9000). The metal dispersion and metal surface area was determined by CO chemisorptions with a pulse chemisorption mode (BELCAT, BEL Japan, Inc.). Samples were treated in He flow by increasing the temperature to 423 K at 5 K min^{-1} and holding at 423 K for 1 h. Samples were then heated to 673 K at 10 K min^{-1} and reduced in 10% H_2/Ar at 673 K for 1 h. Chemisorbed hydrogen was removed by treatment in He flow at 493 K for 1 h. Samples were then exposed to pulses of 5% CO/He. CO concentration was measured using a thermal conductivity detector. Dispersions, defined as the fraction of Pt atoms exposed at surfaces, were determined by assuming one CO standing on one surface Pt atom.

5.1.2 Catalytic reaction

The conversion of cellobiose or cellulose was performed with a batch-type high-pressure autoclave reactor. Typically, 0.050 g catalyst and 0.171 g cellulose (after ball milling for 4 days) or cellobiose were loaded into the reactor pre-charged with 20 mL H_2O. The reactor H_2 pressure was maintained at 5 MPa at room temperature, and

then the reaction was conducted at 463 K for 3 h. After reaction, the solid phase was separated by centrifugation, and the liquid products were analyzed with HPLC (Waters Assoc, USA). Cellulose conversion was determined as reported by the weight difference of dried cellulose before and after the reaction. The cellobiose conversion was calculated through the HPLC results before and after the reaction. The product selectivity was calculated based on the carbon basis. The product yield was calculated as follows: yield (%)=(weight of product)/(weight of cellulose or cellobiose charged in reactor).

5.2 Results and discussion

5.2.1 Characterization of Pt/RGO catalyst

The preparation, the physicochemical properties, and the catalytic performances of Pt/RGO catalyst with the highest catalytic activity were systematically investigated. The morphology of RGO and as-prepared Pt/RGO were characterized with TEM. As in Figure 1, the surface of RGO is smooth and free from any contaminated particulate, which indicates that few layered graphene oxides are formed, although the TEM image cannot estimate the layer numbers of the graphene oxide nanosheets exactly. As in Figure 1(b), highly monodispersed Pt nanoparticles with a uniform size of 3.6 nm decorated on RGO surface are obtained by simple and rapid microwave heating of H_2PtCl_6 and GO in the mixture of EG and water. The most significant feature here is that the Pt nanoparticles with a uniform size (3.6 nm) are well monodispersed on the surface of graphene oxide (as shown in Figures 1(b) and 1(c)). Figure 1(d) is a high-resolution TEM image of Pt/RGO. The measured inter-planar spacing of the particle lattice is 0.23 nm, which corresponds to the (111) crystal plane of Pt nanoparticles given in X-ray diffraction (XRD) data (Figure 5 in Chapter 4). These

TEM images confirm that the highly monodispersed Pt nanoparticles with uniform size can be successfully synthesized and well located on RGO sheets by the microwave assistant reduction method. Compared with previous researches, Pt nanoparticles on graphene oxide sheets seem to be highly monodispersed with smaller uniform size. Furthermore, the Pt/RGO catalyst prepared by microwave assisted reduction method is demonstrated in fluffy state and its surface area is 180.2 m^2/g. The surface area is relatively low compared to the surface area of the single graphene sheet, indicating a certain degree of restacking of the graphene sheets.

X-ray photoelectron spectra (XPS) was used to investigate the surface composition of RGO and Pt/RGO catalysts. As shown in Figure 2, the C1s core level for RGO still shows a high degree of oxidation, which consists of three main components assigned to the C-C (sp^3 carbon, 285.8 eV), C-C (sp^2 carbon, 284.5 eV), C-O (hydroxyl, 286.6 eV) and C=O (carbonyl, 288.4 eV) groups. The large amount of residual functional groups including C-O in RGO indicate that GO was only partly reduced by EG solution. After the introduction of H_2PtCl_6, it is clearly showed that the peak associated with C-C bond (284.5 eV) becomes predominant while the additional peak of C-O (286.6 eV) tremendously decreases, suggesting most oxygen-containing functional groups have been removed. These findings indicate that the addition of H_2PtCl_6 plays an important role in the formation of RGO. Figure 2(c) shows the O1s XPS spectra of RGO and Pt/RGO nanocomposites. The decrease of oxygen-containing functional groups can also be seen from the decreasing peaks of C-O and C=O. Pt 4f spectra of Pt/RGO show the expected doublets for Pt 4f7/2 and Pt 4f5/2, with Pt^0, Pt^{2+}, and Pt^{4+} oxidation states (Figure 2d). It is interesting to note that a respectable percentage of Pt remains in its native state (Pt^0) in Pt/RGO. In addition, two different types of Pt^{2+} can be assigned,

which suggests that the oxygen linkages exist between the Pt nanoparticles and the RGO surface, and the oxide layers formed on the Pt surface. The small Pt nanoparticles are formed by anchoring Pt ion on the graphene oxide surface and by subsequent reduction to the fine particles without obvious agglomeration.

5.2.2 Catalytic performances of Pt/RGO catalyst

The effect of the reaction temperature on the catalytic performance of Pt/RGO catalyst is given in Figure 3. It can be seen that the conversion of cellobiose increases from 75.2 % to 100 % with the temperature increasing from 423 K to 463 K. The sorbitol yield increases simultaneously and reaches the maximum at 463 K, then decreases with the further increasing temperature to 483 K. It is considered that high temperature causes cellobiose to be partially carbonized easily and that the produced sorbitol can be converted further to other undesirable by-products. Consequently, the optimum reaction temperature is 463 K.

When the milled cellulose was used as the raw material, the experimental conditions such as the reaction temperature, the reaction pressure, the reaction time and the Pt concentration were investigated. As shown in Figure 4a, the yield of sorbitol is very low at 423 K. Compared with Figure 3, the low temperature might be not helpful to the hydrolysis of cellulose. The yield of sorbitol and the conversion of cellulose increase with the increasing temperature. However, the sorbitol yield is relatively low when the reaction temperature is 483 K, which might due to the partial decomposition or dehydration of products and the generation of some by-products, such as low molecular polyols, sorbitan, isosorbide, CO and CH_4. The influence of reaction pressure is shown in Figure 4b, from which it can be seen that the conversion of cellulose increases with

increasing pressure. Furthermore, the pressure also has influences on the yield of sorbitol. Higher pressure is helpful to increase the sorbitol yield. The reaction time is also found to be important in this reaction as in Figure 4c. The conversion of cellulose (36.3%) and sorbitol yield are very low when the reaction time for 1 h. However, the conversion of cellobiose is as high as (100 %) when the reaction time is 3 h (Figure 3). The cellobiose is easy to be hydrolyzed compared with cellulose, indicating that the hydrolysis of cellulose is the rate determining step. The effect of Pt loading amount in Pt/RGO catalyst is also studied. The yield of sorbitol can be effectively increase from 24.9 % with 1 wt% of Pt loading to 58.9 % under 5 wt % of Pt loading.

In order to study the stability of Pt/RGO catalyst, the catalyst after 24 h reaction was characterized with TEM. As shown in Figure 5, the average size of Pt nanoparticles on the used Pt/RGO catalyst is similar to that of the fresh one. Particle aggregation is not observed in the TEM image, suggesting that the catalyst is very stable and can be reused. In Figure 6, the reusability also can be proved by the similar sorbitol selectivity with the used Pt/RGO as catalyst and fresh cellulose as reactant. The slight decrease of cellulose conversion after several runs might be due to the loss of catalysts during the transfer process.

5.2.3 Reaction mechanism of cellulose conversion

The enhanced catalytic performance of Pt/RGO catalyst for the conversion of cellulose to sorbitol may be due to the following reasons: The increase in utilization efficiencies of platinum nanocatalysts on RGO supports can be attributed to the enlarged surface area and the well-dispersion of the RGO supports and catalyst. The optimum size of Pt particles and the exposed crystal plane are beneficial for the

hydrogenation of reactants. Pt on RGO promotes the protonations of water and hydrogen molecules, which spill over to create in situ acid sites, and to catalyze hydrolysis of cellulose or cellobiose (Scheme 1), and the intermediate glucose or other oligosaccharides can be selectively hydrogenated to sorbitol on the highly active Pt nanoparticles. Therefore, the roles of the RGO in the conversion of sugars to sorbitol were acting as a support to highly disperse Pt by anchoring effect, keeping surface acid by H_2 spillover effect from Pt, catalyzing hydration reaction by its acidic sites, suppressing formation of by-products.

5.3 Conclusion

Pt/RGO catalyst is prepared by microwave assistant EG reduction method, which presents high activity and selectivity for the conversion of cellobiose or cellulose to sorbitol. The structure and the catalytic performance of Pt/RGO catalyst are systematically investigated. The high catalytic activity is attributed to the synergistic effects of supports and the supported Pt nanoparticles. The results show that the graphene oxide sheets act as an excellent support and stabilizer for the very finely dispersed Pt nanoparticles, which can avoid nanoparticle aggregation. The sorbitol yield is as high as 91.5 % or 58.9 % when cellobiose or cellulose employed as the reactant, respectively. The optimum particle size of Pt is 3.6 nm and the optimum reaction temperature is 463 K. The improvement of catalytic activity is attributed to the hydrogen spillover effects of Pt/RGO catalyst.

Figures and Schemes

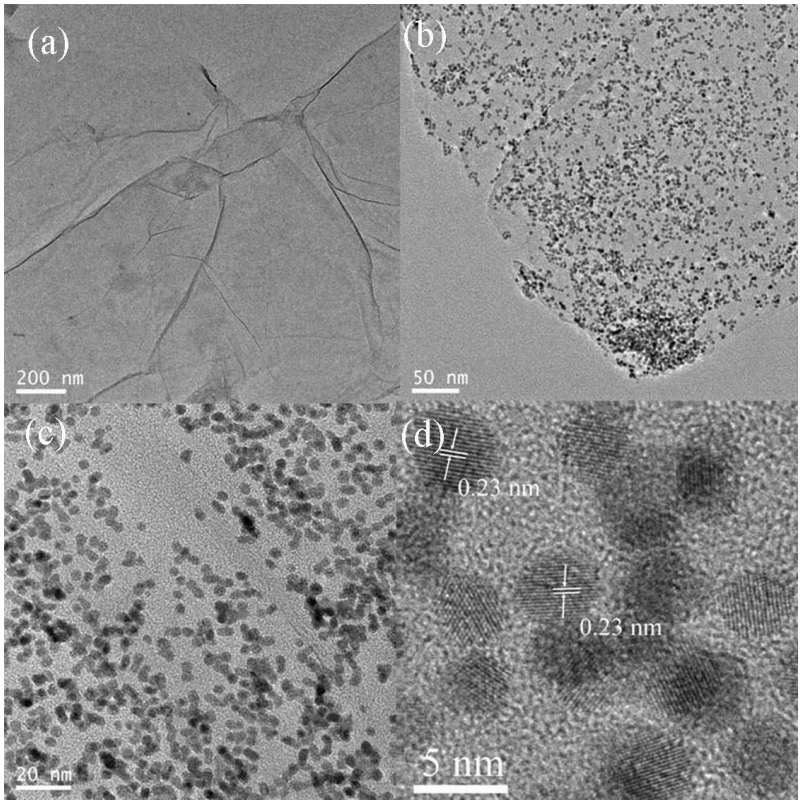

Figure 1. TEM images of (a) RGO, (b, c) Pt/RGO, and (d) high-resolution transmission electron microscopy (HR-TEM) image of Pt/RGO.

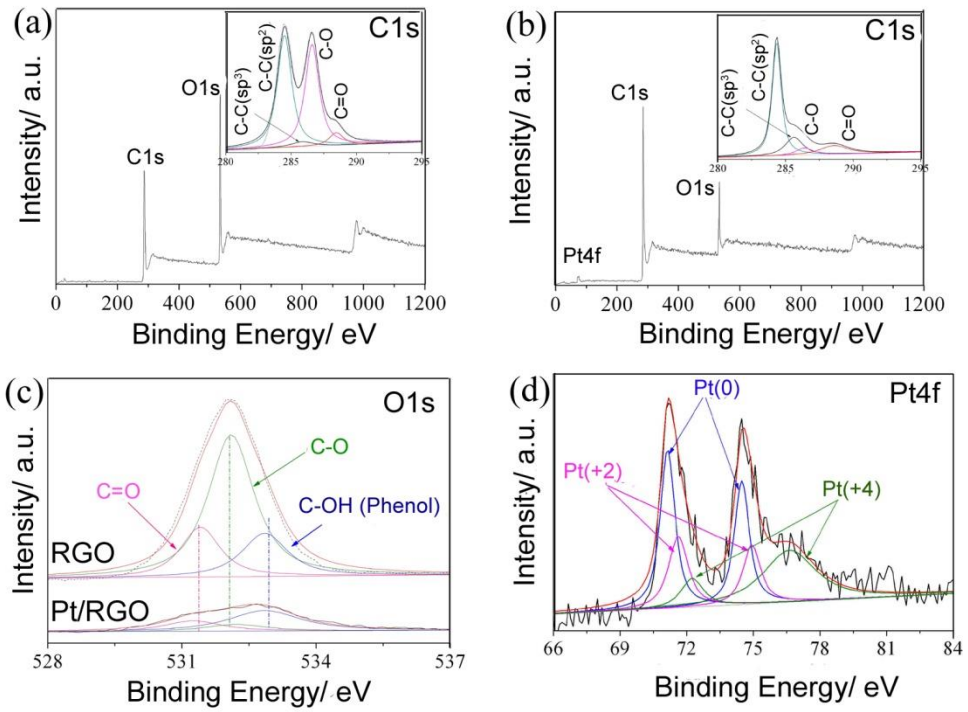

Figure 2. Typical XPS spectra of RGO and Pt/RGO: (a) survey spectra and C1s of RGO, (b) survey spectra and C1s of Pt/RGO, (c) O1s region XPS spectra, and (d) Pt4f region XPS spectra.

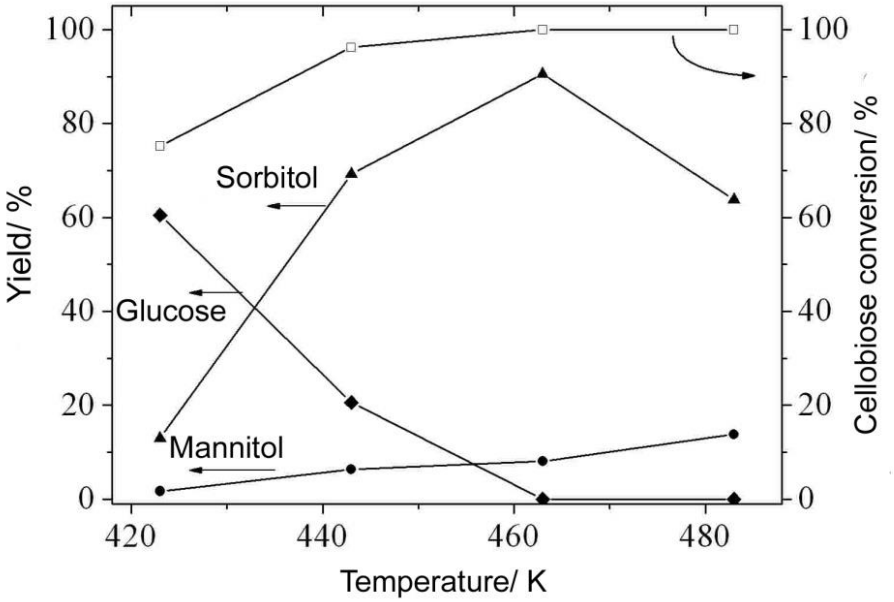

Figure 3. Influence of the reaction temperature on the conversion of cellobiose to sorbitol. (Reaction conditions: Catalyst weight =0.050 g; Cellobiose weight =0.171 g; Reaction time= 3 h; Temperature=423-483 K; Pressure=5 MPa; H_2 as reaction gas.)

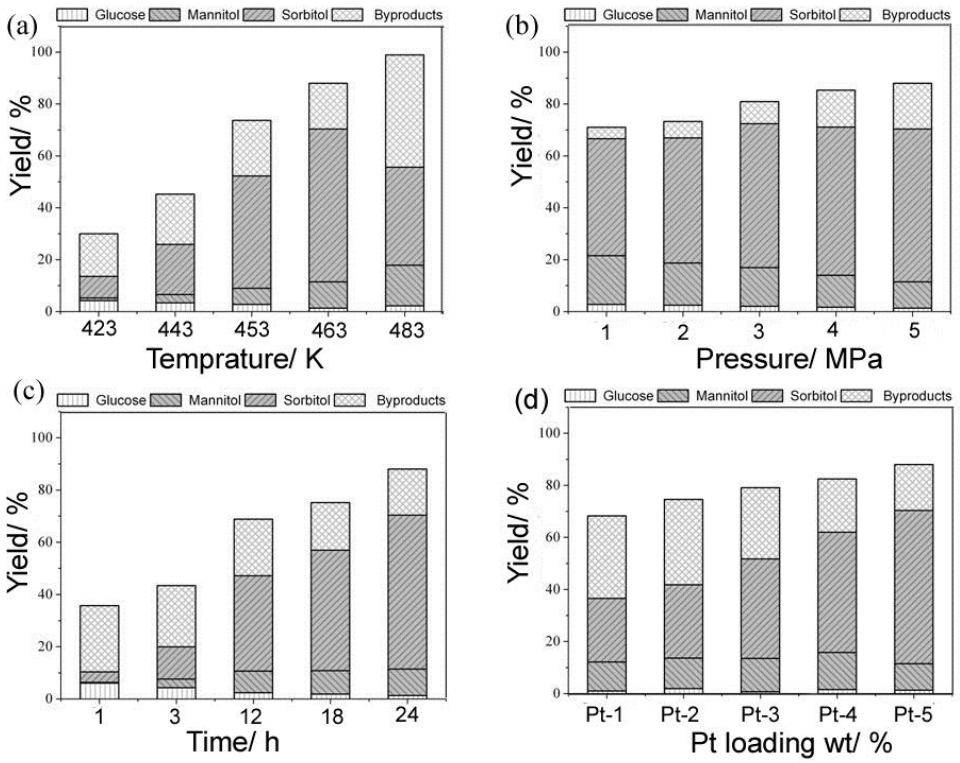

Figure 4. Influences of (a) reaction temperature, (b) reaction pressure, (c) reaction time and (d) Pt loading amount on the conversion of cellulose to sorbitol. (Reaction conditions: Catalyst weight =0.050 g; Cellulose weight =0.171 g; H_2 as reaction gas; Temperature=463K, (a, 423-483 K); Pressure=3MPa (b, 1-5 MPa); Reaction time=24 h (c, 1-24h); Pt loading amount=5% (d, 1%-5%).)

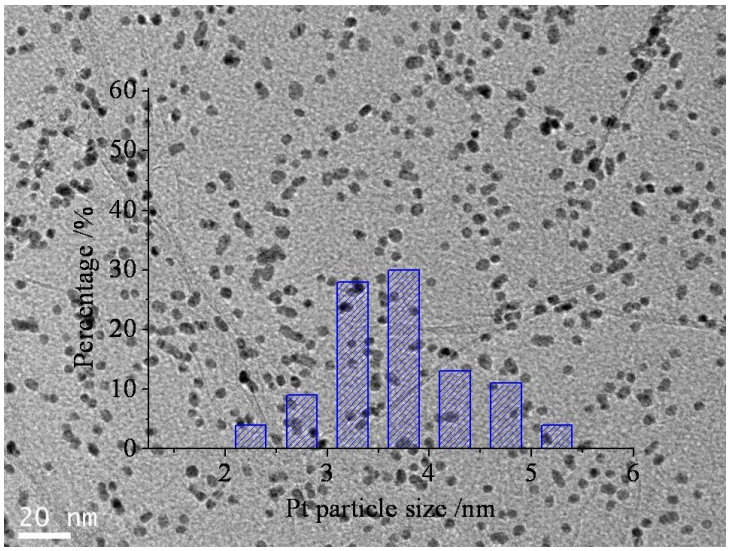

Figure 5. TEM image of the used Pt/RGO catalyst in the conversion of cellulose to sorbitol. (Reaction conditions: catalysts weight =0.050g; Cellulose weight =0.171 g, Reaction time= 24 h; Temperature=463 K; Pressure=5 MPa; H_2 as reaction gas.)

Figure 6. Reuse experiments of Pt/RGO catalyst for cellulose conversion. (Reaction conditions: catalysts weight =0.050 g; Cellulose weight =0.171 g, Reaction time= 24 h; Temperature=463 K; Pressure=5 MPa; H_2 as reaction gas.)

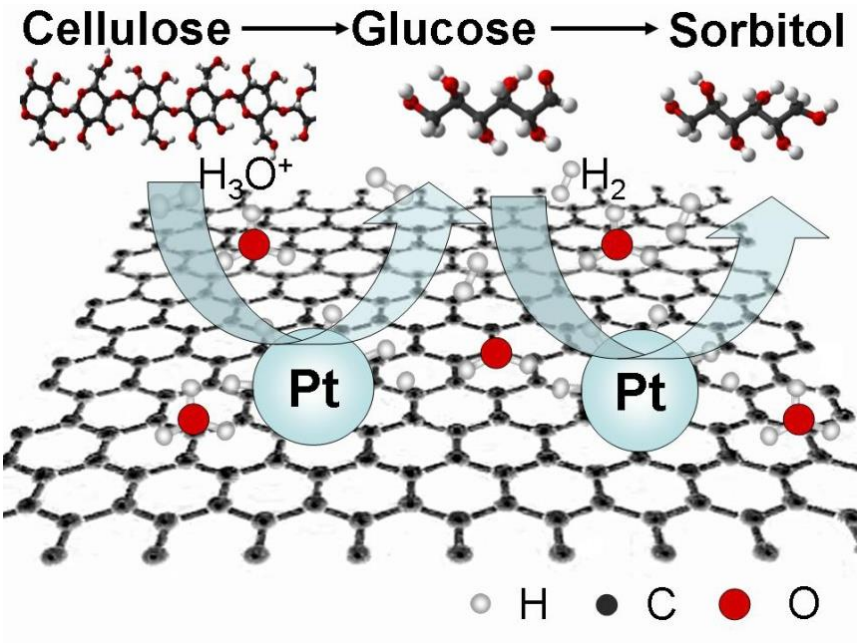

Scheme 1. Schematic of the conversion mechanism for cellulose to sorbitol catalyzed by Pt/RGO.

Section III Conversion of Syngas to Isoparaffins

Chapter 6 Combining Wet Impregnation and Dry Sputtering to Prepare Highly- Active CoPd/H-ZSM5 Ternary Catalysts Applied for Tandem Catalytic Synthesis of Isoparaffins

6.1 Abstract

Tuning hydrocarbons distribution in Fischer-Tropsch synthesis is greatly challenging. By employing three different pathways to deposit trace Palladium on Co/H-ZSM5 catalyst, tunable isoparaffin and olefin selectivity was successfully achieved. The impregnated Pd showed a poor promotion of Co dispersion and reducibility, producing a slight enhancement of FTS activity and isoparaffin selectivity. The unique mechanical stir during Pd sputtering induced a re-dispersion of impregnated Co/H-ZSM5 particles and Pd was deposited with an intimate distance to Co species and with a weak interaction combining zeolite, due to which complete hydrogenation of olefins was achieved. The surface enriched Pd on pre-sputtered Co catalyst was inclined to form Pd-Co nano-alloys, suppressing the chain growth activity by excessive hydrogenation process.

Keywords: Fischer-Tropsch synthesis; sputter; palladium; isoparaffin; olefin.

6.2 Introduction

For a multifunctional catalyst containing three components (A+B+C) or more, optimizing the spatial arrangement and interactions between different active sites is greatly crucial to achieve a high catalytic performance and selectivity of expected products. Based upon a typical Fischer-Tropsch synthesis (FTS),[66-69] it is one of the most efficient processes to produce synthetic gasoline-ranged hydrocarbons from CO and H_2 by combining a FTS metal (Co/Fe/Ru, component A) and an acidic zeolite (component B) as a bi-component catalyst. The efficient isoparaffin synthesis from FTS has moved into the spotlight since the rapidly increasing energy demand worldwide turns the sustainable energy production into one of the greatest challenges.[70]

A general strategy to assemble such bi-component catalyst is realized by a physical mixture method of two different components or a wet impregnation of component A into component B.[71, 72] However, the contact between two components on the physical mixture process is usually far from each other. Deposited FTS active sites over conventional impregnated catalysts are randomly distributed on surface and strongly interacted with the acidic zeolite, showing a difficult reduction of active metals. In addition, for the acidic catalysis process on zeolite supported FTS catalysts, isomerization and hydrocracking of normal paraffins are primary reactions, in which formation of many olefin products is unavoidable besides saturated paraffins. Therefore, an additional hydrogenation promoter as component C is necessary to be introduced for producing more saturated chain and branch hydrocarbons. Introduction of trace noble metals, such as Ru, Re, Pt and Pd, is regarded as an effective way to realize such purpose accompanied by a possible promotion of metal dispersion, reduction degree and catalytic performance.[73-76] For the consecutive reactions above, there is no doubt that

great challenges still remain in fabrication of these types of active sites, including a FTS metal, acidic sites and a noble metal promoter, into one efficient catalyst system with an optimized spatial arrangement and suitable interactions.

Recently, the newly developed physical-sputtering method provided a novel route to deposit various metal nanoparticles onto powder supports.[77-79] The unique mechanical vibrating and rotation during sputtering produced well-dispersed metal sites, intimately contacting acidic sites on zeolite support. The interaction between two components is clearly weakened as compared to conventional impregnated catalyst.

In present work, we design three metal deposition pathways to prepare zeolite supported Pd-Co catalysts for effective production of isoparaffins from CO and H_2. Cobalt, a FTS site, and palladium, a noble metal promoter were deposited on H-ZSM5 support by a single chemical impregnation route, a single physical sputtering method or a hybrid process of the two above, respectively. By adjusting the metal introduction pathways, different catalytic performance and tunable distribution of isoparaffins and olefins were obtained. Correlations between FTS results of catalysts and their unique physicochemical properties were investigated in detail.

6.3. Experimental Section

6.3.1 Catalyst preparation of three Pd-promoted Co/H-ZSM5 catalysts

The CoPd-ii catalyst was prepared by a conventional co-impregnation process of the commercial H-ZSM5 support (Süd-Chemie Catalysts Japan Inc., SiO_2/Al_2O_3=100, molar ratio). Prior to the impregnation experiment, H-ZSM5 powders were pretreated at 180°C for 2 h in air followed by cooling down to room temperature. Briefly, analytical grade $Co(NO_3)_2 \cdot 6H_2O$ powders (Kanto Chemical Co. Inc., Japan) and $Pd(NO_3)_2$ solution (Pd content: 50 $g \cdot L^{-1}$, Tanaka Noble Metal Co., Japan) were dissolved in

distilled water (10 mL) to form a hybrid solution, followed by impregnation of the aqueous solution onto the pretreated H-ZSM5 powders (3.0 g). After an ultrasonic mixing for 30 min, the precursor mixture was aged in humid air for 12 h. Then, it was dried at 80 °C under vacuum, and calcined at 400°C for 2 h in air. The weight loading was 6.0 % and 0.5 % for Co and Pd, respectively.

For the CoPd-is one ("is" means Co impregnation followed by Pd sputtering), impregnated Co on H-ZSM5 support was first prepared by incipient wetness impregnation method. The obtained Co/H-ZSM5 catalyst served as a Pd sputtering support. The sputtering apparatus was described in Scheme 1. A metallic palladium plate (99.9%, 50×100 mm^2, Toshima Ltd.) was used as a sputtering target. Briefly, 3.0 g of the Co/H-ZSM5 powders and a rectangle stainless steel as stirrer were loaded into the cavity barrel. Afterwards, the vacuum chamber was evacuated to 9.9×10^{-4} Pa, followed by introducing a pure argon flow (purity: 99.995%) with a flow rate of 13 $mL\cdot min^{-1}$ into the chamber until the pressure reached 2.0 Pa. The input power was controlled to 45 W. A swinging motion of $\pm75^{o}$ at a speed of 4.2 rpm was provided for the rolling barrel during the sputtering process, achieving a uniform deposition of metal atoms on support. After 15 min sputtering, around 0.5 wt% of Pd was deposited. Finally, a 1% O_2 flow (balanced with N_2) was gradually introduced into the cavity barrel to reach room pressure.

For the CoPd-ss one, Co was first deposited on the H-ZSM5 support by the sputtering method with a metallic Co target. The input power and sputtering time were controlled to 350 W and 2.5 h, respectively. Afterwards, Pd was introduced on the as-sputtered Co/H-ZSM5 with the same sputtering conditions as for the CoPd-is catalyst. The weight loading amount of Co and Pd were controlled to 6.0% and 0.5% for all above three

Pd-containing catalysts.

For comparison, two reference Co/H-ZSM5 (Co: 6.0 wt%) bifunctional catalysts without palladium were prepared by the impregnated (Co-i) and sputtered (Co-s) method, respectively. Another reference Pd/H-ZSM5 catalyst (Pd: 0.5 wt%) without cobalt (Pd-i) was prepared by the impregnation method as well.

6.3.2 Catalyst characterization

FEI Tecnai F20 high-resolution transmission electron microscope (HRTEM) with an accelerating voltage of 200 kV was used for the metal distribution morphology, and Digital Micrograph software was employed to acquire fast Fourier transforms (FFT) images.

A JEOL energy-diffusive X-ray spectroscopy (EDX) was used for element analysis.

X-ray diffraction (XRD) analysis was performed on a Rigaku RINT 2400 diffractmeter with Cu Kα radiation operated at 40 kV and 20 mA.

A BELCAT-B-TT apparatus (Bel Japan Inc.) was employed to perform the H_2 temperature-programmed reduction (H_2-TPR) and NH_3 temperature-programmed desorption (NH_3-TPD) experiment at a heating rate of $10°C \cdot min^{-1}$.

The metal dispersion was determined by a H_2 chemical adsorption experiment performed with Autosorb-1 vacuum apparatus. Samples of about 50 mg were placed in a quartz cell. Prior to the measurement, the samples were degassed at 300 ºC and at 3.0 Pa for 1 h. The impregnated catalyst was reduced in flowing H_2 at 400 ºC for 10 h, and evacuated at 400 ºC for 1 h to desorb H_2, followed by cooling to 100 ºC. The chemical adsorption was conducted at 100 ºC and the equilibration time was 30 min. Co dispersion was calculated assuming that an H/Co adsorption stoichiometry was equal to

1.

To determine the reduction degree of the prepared catalyst, the O_2 titration experiment was carried out at 400 ^oC using the catalyst analyzer BELCAT-B-TT with the assumption that the metallic Co atoms were oxidized totally to Co_3O_4.

6.3.3 Evaluation of FTS performance

Prior to FTS reactions, all the catalysts were *in situ* reduced in the reactor at 400^oC for 10 h with a pure H_2 flow. Details of the FTS steps were described elsewhere.[78, 90] Briefly, the FTS reaction was performed with a continuous flowing fixed-bed reactor from syngas (CO: 33.7 v%, Ar: 3.04 v%, balance with H_2). An ice trap of n-octane as solvent was equipped to capture the heavy hydrocarbons in the effluent. Reaction conditions were 260 °C, 1.0 MPa, and $W_{catalyst}/F$ = 10 g·h·mol^{-1}. Gas products (C_1-C_5) were analyzed by two on-line gas chromatographs, one of which employed an active charcoal column equipped with a thermal conductivity detector (Shimadzu, GC-8A). Another used a capillary column (J&W Scientific GS-Alumina) and a FID detector (Shimadzu, GC-14B) to analyze light hydrocarbons. Liquid products from the ice trap were analyzed by an offline gas chromatograph using a FID detector (Shimadzu, GC-2014).

6.4 Results and Discussion

6.4.1 Metal dispersion

HRTEM images and particle size distributions (PSD) of prepared catalysts are provided in Figure 1. The Co species loaded by a conventional impregnated method (Co-i) show irregular and heterogeneous large particles with an average particle size of 19.3 nm, as counted in Figure 1a2. For the CoPd-ii catalyst prepared by co-impregnated

way, a similar metallic particle distribution ranging from 11 to 24 nm was observed. The corresponding fast Fourier transforms (FFT) image indicated that both of Co and Pd species existed in oxide state. In contrast, the impregnated Co/H-ZSM5 catalyst followed by a Pd-sputtering process exhibited a clear promotion of particle dispersion (Figure 1c) accompanied by a narrow particle distribution of 4-9 nm. The result revealed a "stir" role of the sputtering method, in which a continuous hexagonal rotation and mechanical vibration powered by the apparatus were able to mix the deposited metals and powders support adequately. Simultaneously, a small stirrer in the rolling barrel further provided additional power to break impregnated Co/H-ZSM5 bulks into a mass of small uniform particles. Therefore, a re-dispersion of Co/H-ZSM5 large particles was observed assisted by the rolling, vibration and stirrer during the sputtering process. In addition, the FFT image of Figure 1c1 demonstrated typical Co_3O_4 (400), (311) and (111) lattice planes with the absence of Pd oxide species, illustrating a high dispersion of sputtered Pd on Co/H-ZSM5 support or the formation of tiny Pd nanoparticles.

The uniform dispersion of small Co and Co-Pd particles on the sputtering-only catalysts is reflected by Figure 1d and 1e. It was observed that particle distributions on the sputtered CoPd-ss and Co-s catalysts were close. Both of the average particle sizes on these catalysts were about 3.9 nm, much smaller than that of CoPd-ii or CoPd-is, due to which no metallic lattice planes were found except the zeolite support in Figure 1d1. This result was further confirmed by the XRD spectra (ESI, Figure S1). But two kinds of sputtered Co and Pd nanoparticles were active and facile to form alloys with different ratios owing to the active metallic property,[81] and the interaction between two metallic atoms was enhanced compared to the other two Pd-containing catalysts CoPd-ii and

CoPd-is. Furthermore, the surface enrichment of sputtering led to the Pd coverage on top of active cobalt species. These reasons could produce a possible decrease of the C-C chain growth activity on cobalt sites as compared to monometallic Co/H-ZSM5 catalyst.

6.4.2 XPS analysis

To investigate the metallic state and interaction between Co and Pd, XPS measurements were performed and shown in Figure 2. All the catalysts were *in situ* pre-reduced with a H_2 flow of 5% under 400°C for 5 h in the pretreatment chamber before XPS determinations. Due to its metallic property as reported in literatures,[79] the sputtered CoPd-ss catalyst was pre-calcined in air for comparison with other impregnated catalysts before the *in situ* reduction XPS. For the Co 2p spectra, the peaks at around 781.5 and 777.9 eV were generally attributed to the Co(II) and metallic Co(0) species, respectively.[82,84] All the Pd-promoted catalysts were composed of Co(0) and Co(II), however, the ratio of two phases was different. As shown in Table 1, the sputtered CoPd-ss showed the highest metallic Co content, higher than other two impregnated ones, indicating a more facile reduction behavior on sputtered Co-based catalyst. All the Pd introduced Co/H-ZSM5 showed an increased Co(0)/Co(II) ratio as compared to the unpromoted Co-i one, which was attributed to the enhanced reduction ability due to the hydrogen spillover effect from palladium onto cobalt species.

For the Pd 3d spectra, the doublet binding energy (BE) peak at 334-335 and 339-340 eV was ascribed to the metallic Pd(0) species.[84,85] The three Pd-promoted ternary catalysts showed different binding energy value of metallic Pd, which followed the order of CoPd-ii > CoPd-ss > CoPd-is. It was notable that the lowest BE peak of Pd at 334.1 eV occurred on the CoPd-is one with a hybrid introduction pathway of cobalt and

palladium, corresponding to the weakest physical force between Pd and Co/H-ZSM5. The co-impregnated catalyst showed the highest one, which was ascribed to the strong intermetallic force of Pd-Co and the strong interaction between metals and H-ZSM5 support. The BE value of metallic Pd on the CoPd-ss one was between the two above, indicating that the intensity of interaction was between strong metal-support interaction and weak physical force as well. Therefore, we attributed such BE peaks to an alloying Pd species, which were easily bonded with the active sputtered Co by a Pd-Co alloying force.[85] Accordingly, the different palladium binding energy accounted for different interactions of three ternary catalysts.

The comparison of Co/Pd ratio from EDX and XPS on different catalysts is shown in Table 1. The latter reflects the surface element composition due to the detection depth in nano-scale. The Co/Pd ratio value from XPS on CoPd-ss catalyst is 11.1, close to the theoretical value of EDX result. It is known that the physical sputtering is a surface enrichment process of deposited metals. All of the deposited metals were uniformly dispersed on the surface of H-ZSM5. For the CoPd-is catalyst, the lowest Co/Pd ratio among three catalysts was attributed to the surface Pd-sputtering process, in which Pd atoms were greatly enriched on the Co/H-ZSM5 support. The various Co/Pd ratios from XPS indicated the different nature of three Pd introduction pathways.

6.4.3 H_2-TPR analysis

H_2-TPR curves of different prepared catalysts are presented in Figure 3. For the impregnated Co-i catalyst, a two-stage H_2 consumption at 295 and 385°C was assigned to a typical reduction of Co_3O_4 to CoO ($Co_3O_4+H_2 \rightarrow 3CoO+H_2O$) and that of CoO to the metallic cobalt ($CoO+H_2 \rightarrow Co^0+H_2O$).[21] The tailing H_2 consumption signal towards

a higher temperature (more than 700°C) indicates a strong interaction of metallic Co and zeolite support, and this portion of Co species are difficult to reduce. For three Pd-containing catalysts, the co-impregnated catalyst revealed three H_2 consumption peaks at 126, 290 and 770°C, respectively. The lowest one was supposed to be due to the reduction of cobalt around noble metals,[75] while the highest one was assigned to the strong interaction between metallic species and H-ZSM5. Clearly, Pd introduction by the common impregnated way was not able to efficiently promote the reduction of those cobalt oxides which was difficult to be reduced at common temperature (below 400°C).

For the two sputtered Pd-containing catalysts, it is important to point out that the absence of H_2 consumption at higher than 700°C and a clear decrease reduction temperature from 770 to 650°C are indicative of a weakness of the interaction between metals and zeolite. A reason is that highly-dispersed Pd atoms transferred hydrogen atoms to cobalt oxide species, promoting the hydrogen dissociation process on surface of cobalt clusters nearby. Here, the role of impregnated and sputtered palladium was different. The former helped to decrease the reduction temperature of cobalt oxides adhered to palladium, and the latter was able to reduce those cobalt species strongly bonded with zeolite. In addition, a small negative peak at about 100°C was observed on the CoPd-is catalyst, demonstrating the reduction of palladium oxide and $COPdH_x$ decomposition.[87] This peak was also observed on the reference Pd-only catalyst, but not found on the CoPd-ss one, because of the possible Pd-Co alloy formation on the latter. The result was in accordance with XPS analysis.

The reducibility promotion was further confirmed by the Co reduction degree determined by a O_2 titration method (Table 2). In contrast to the unpromoted Co-i, a more obvious promotion of reduction degree and metal dispersion was observed on the

CoPd-is catalyst than on the CoPd-ii, which was also comparable to that of the sputtered monometallic or bimetallic catalysts. Besides, the dispersion result from chemisorption was in well accordance with HRTEM analysis, further confirming the optimized spatial arrangement of Co nano-clusters. The addition of palladium on the sputtered cobalt catalyst slightly decreased the metal dispersion, resulting from the Pd-Co alloy formation or surface cover of the subsequent Pd sputtering layer.

6.4.4 Acidic sites distribution

For the consecutive reaction from syngas to isoparaffins, distribution of acidic sites on zeolite is also important to fabricate a highly-selective ternary catalyst. NH_3-TPD curves of different prepared catalysts were illustrated in Figure 4. The ammonia desorption at a low temperature of 120-230°C was associated with the weakly bonded NH_3 molecules, and the higher one at about 250-500°C was related to the strong Brønsted acidic sites.[88] It is worth mentioning that the strong acidic sites on three impregnated Co catalysts (Co-i, CoPd-ii and CoPd-is) were extended toward a higher temperature as compared to raw H-ZSM5. No obvious alternation was observed after Pd addition, due to its low loading amount. The estimated total NH_3 uptake (listed in Table 2) indicated that the Pd introduction by the sputtering method could reserve more acidic sites and its acidic distribution is closer to that of the raw zeolite than that by conventional impregnated way. The possible reason for this result is the different interaction between deposited metals and zeolite.[78] The strong interaction between impregnated metals and zeolite promoted the formation of Al-O-M structure (M = Co or Pd), and thus more acidic sites from Al species were covered. But the weakly physical force in the sputtered one could expose more Al sites on the support, which was

responsible for acidic sites. This was in favour of more isomerization hydrocarbons produced in FTS experiment.

6.5 FTS performance: tuning isoparaffin and olefin selectivity by different Pd introduction ways

FTS performance of different prepared catalysts and product distribution are presented in Table 3 and Figure 5. Clearly, both of the impregnated and sputtered Pd on impregnated Co/H-ZSM5 are able to promote the CO conversion. The Pd sputtered on Co/H-ZSM5 catalyst exhibited the most obvious promotion effect on the FTS activity, which was ascribed to evolution of metal distribution achieved by the re-dispersion of metal particles during sputtering. Whereas for the CoPd-ss catalyst, the CO conversion clear decreased due to the surface coverage of Pd atoms on top of Co species and the Pd-Co nanoalloys formation.

For the product distribution, the co-impregnated CoPd-ii slightly enhanced the isoparaffin selectivity and lowered the olefin selectivity, owing to the hydrogenation on Pd promoter. In contrast, the olefin to *n*-paraffin ratio on the CoPd-is catalyst was clearly decreased to 0.07 from 0.81 on the unpromoted Co-i, demonstrating that the sputtered Pd on Co/H-ZSM5 almost converted all unsaturated hydrocarbons to saturated branced and normal paraffins. The hydrogenation role was promoted more effectively on the sputtered Pd catalyst rather than on the impregnated one. More reserved acidic sites on the CoPd-ss and Co-s catalyst were responsible for the highest *iso*- to *n*-paraffin ratio. However, the enhanced CH_4 and C_{2-4} selectivity as well as decreased C_{5-11} and C_{12+} selectivity were found on the CoPd-ss catalyst as compared to the unpromoted Co-s one, suggesting a suppression of the chain growing FTS reaction and excessive conduction of the hydrogenation process on the Pd-covered Co species. The result was

probably ascribed to surface coverage of Pd atoms and enhanced interaction between Pd-Co nanoalloys. The arrangement of Pd and Co clusters on CoPd-ss is different from that on the CoPd-is, where the cobalt clusters of CoPd-is were dispersed both on surface and in bulk of the acidic zeolite. The contact between surface enriched Pd and re-dispersed Co was suitable in the consecutive chain growth reaction and hydrogenation process, as in CoPd-is.

The unsaturated alkenes produced from FTS reaction and hydrocracking can arrive at the well-dispersed palladium sites as a hydrogenation center nearby, achieving a highly-effective tandem reaction including a FTS reaction, isomerization, hydrocracking and hydrogenation process in one well-designed ternary catalyst (Scheme 2). The yield of isoparaffin on the CoPd-is catalyst reached the highest value of 30.1% among all the five catalysts in consideration of both activity and selectivity. Therefore, in this study, the hybrid introduction of sputtered Pd and impregnated Co on H-ZSM5 is the best way to produce isoparaffins efficiently from syngas.

6.6 Conclusions

Zeolite supported Pd and Co clusters were successfully deposited by three combined methods, including the impregnation-only, sputtering-only and novel hybrid process. For the impregnation-only CoPd-ii catalyst, large particles of Co/Pd were randomly distributed and a slight promotion of Co dispersion and reduction degree were observed, resulting in mere promotion of activity and saturated *iso*- or *n*-paraffin selectivity in the FTS reaction; For the sputtering-only CoPd-ss, surface enriched Pd covered and occupied partial surface of sputtered Co sites, combining Co nanoparticles with an alloy force. The chain growth reactions were suppressed by the hydrogenation role on Pd sites.

For the hybrid CoPd-is achieved by Co impregnation and Pd sputtering on H-ZSM5, the re-dispersion of impregnated Co during Pd sputtering contributed to a striking promotion of dispersion, producing suitable contact between Co and Pd. The hydrogenation role was optimized and the highest yield of isoparaffin was realized on such hybrid ternary catalyst by suppressing olefin production. The novel hybrid route of bimetallic introduction extended the application of sputtering method and provided an efficient strategy in utilizing trace noble metals for promoting production of gasoline-ranged hydrocarbons.

Schemes and Figures

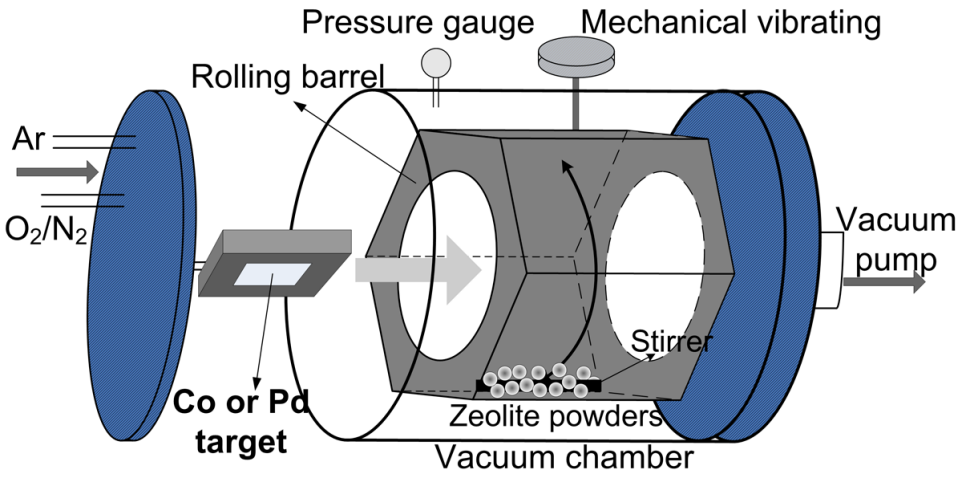

Scheme. 1 Schematic representation of the sputtering apparatus.

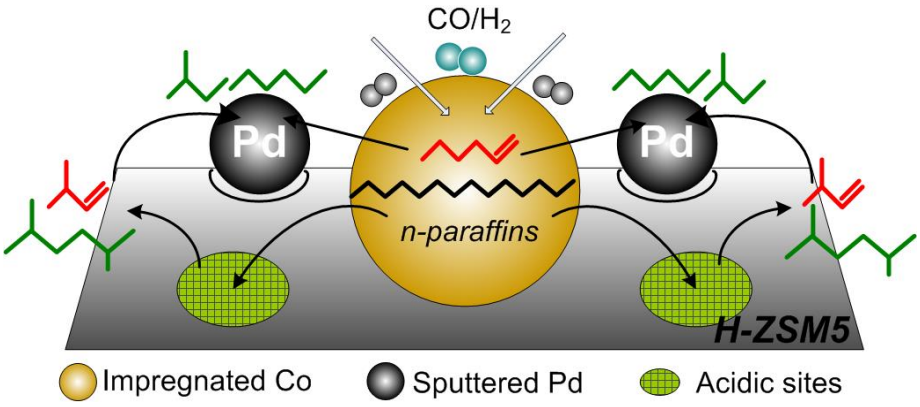

Scheme. 2 Schematic representation of the catalysis process on the ternary Pd-Co/H-ZSM5 catalyst.

Table. 1 The ratio of Co/Pd and Co(0)/Co(II) on different Pd-promoted catalysts

Catalyst	Co/Pd (weight ratio)		Co(0)/Co(II) from XPS
	EDX	XPS	
Co-i	—	—	0.27
CoPd-ii	12.0	8.9	0.40
CoPd-is	12.0	5.4	0.41
CoPd-ss	12.0	11.1	1.12

Table. 2 Properties of the prepared catalysts

Catalyst	D_{Co}[a] %	R_{Co}[b] %	NH_3 uptake[c] /mmol·g^{-1}	d (Co^0)[d] /nm	d (TEM) /nm
Co-i	5.3	45.3	2.10	18.1	19.5
CoPd-ii	8.8	51.1	1.80	10.9	16.7
CoPd-is	15.4	66.9	1.90	6.2	6.3
CoPd-ss	14.1	75.2	2.20	6.8	3.9
Co-s	17.2	70.1	2.20	5.6	3.8

[a] Dispersion of Co: calculated from H_2 chemisorption results.
[b] Reducibility of Co: calculated from H_2-O_2 titration by BELCAT equipment.
[c] Measured by NH_3-TPD curves.
[d] d (Co^0): Co^0 particle size calculated from d= 96/D_{Co}%.

Table. 3 FTS performance of different prepared catalysts

Catalyst	CO Conv. [a] %	Selectivity (C-mol %)				C_{iso}/C_n [b]	C_{ole}/C_n [c]	Y_{iso} %[d]
		CH_4	C_{2-4}	C_{5-11}	C_{12+}			
Co-i	53.4	22.9	18.0	55.1	4.0	0.93	0.81	11.1
CoPd-ii	64.1	25.0	20.2	52.0	2.8	1.39	0.34	18.6
CoPd-is	80.1	20.6	22.1	55.1	2.2	1.51	0.07	30.1
CoPd-ss	46.7	22.7	27.9	46.5	2.9	1.60	0.02	16.9
Co-s	63.0	15.6	10.4	66.3	7.7	2.14	0.63	27.3

[a] Obtained by the stable status. Reaction conditions: 260°C, 1.0 MPa, and $W_{catalyst}/F = 10\ g \cdot h \cdot mol^{-1}$.

[b] C_{iso}/C_n is the molar ratio of all isoparaffins to all normal paraffins with n>3.

[c] C_{ole}/C_n is the molar ratio of olefin to all normal paraffins with n>1.

[d] Y_{iso} stands for the yield of isoparaffin (Y_{iso}=conversion × isoparaffin selectivity).

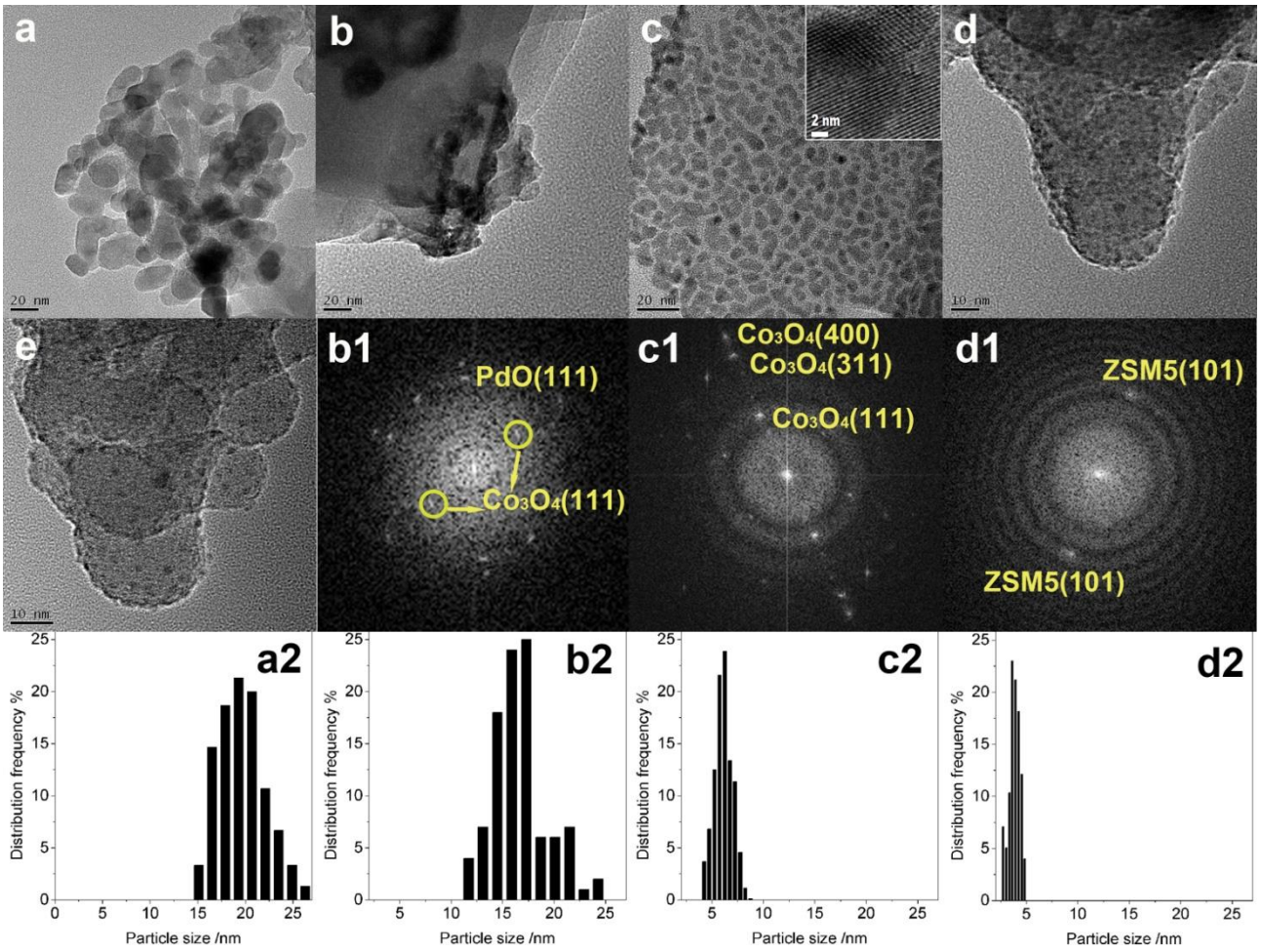

Figure. 1 HRTEM images: a) Co-i; b) CoPd-ii; c) CoPd-is; d) CoPd-ss; e) Co-s, b1-d1) the fast Fourier transforms (FFT) images of selected area on b-d, a2-d2) particle size distributions (PSD) obtained from TEM a-d.

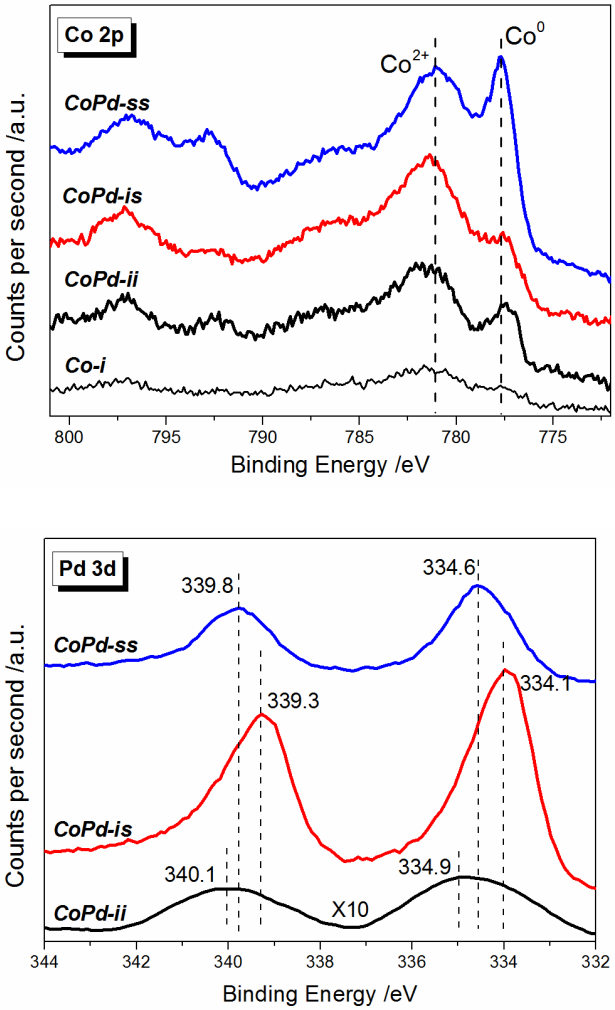

Figure. 2 XPS spectra of Co 2p and Pd 3d level of various Co/Pd catalysts

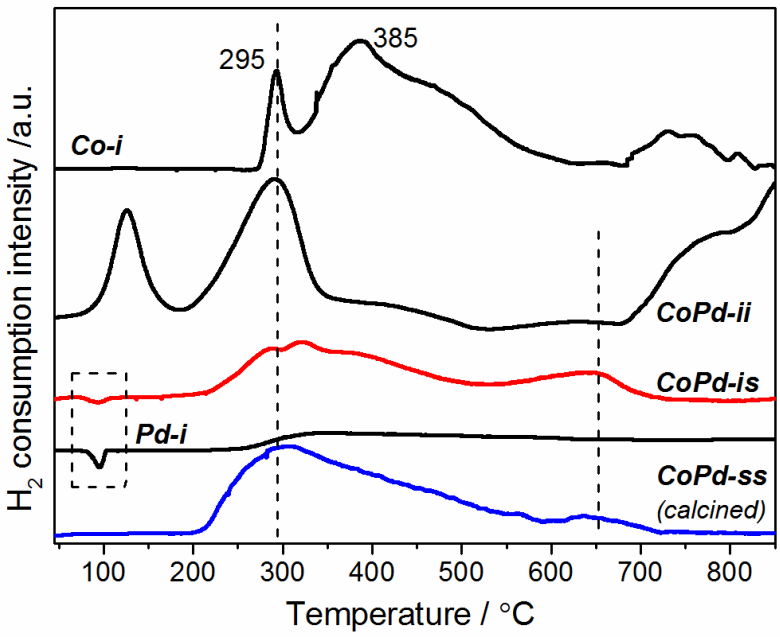

Figure. 3 H_2-TPR curves of different prepared catalysts.

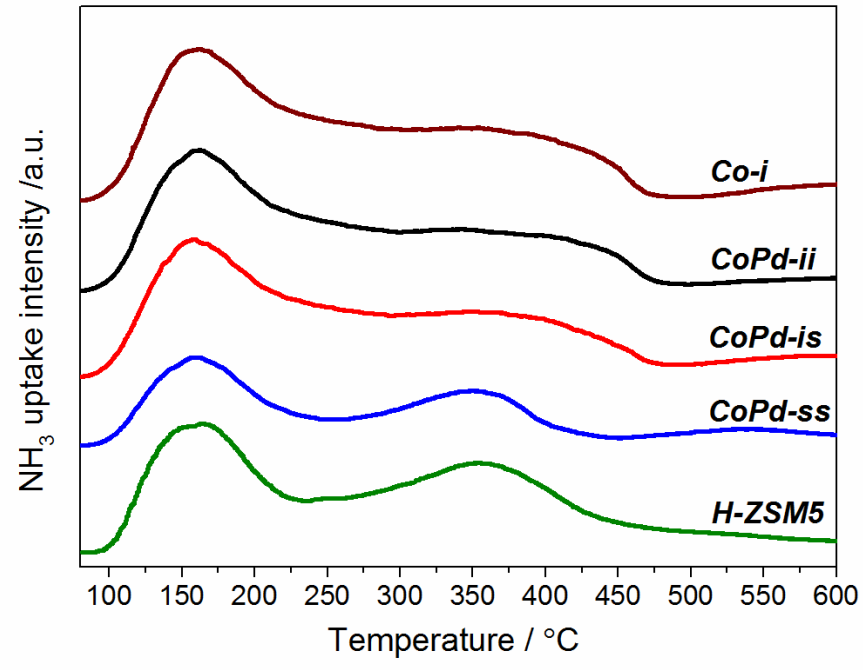

Figure. 4 NH_3-TPD curves of different prepared catalysts.

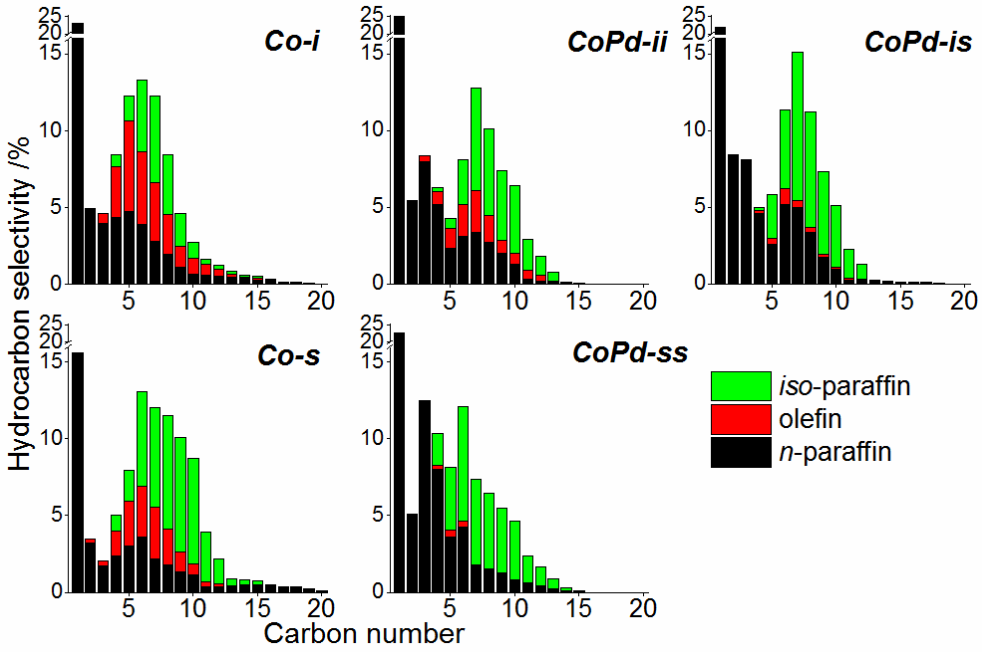

Figure. 5 FTS Product distributions of prepared catalysts.

Chapter 7 Conclusion

In this doctoral dissertation, Biomass derived 5-hydroxymethylfurfural (HMF), cellulose, cellubiose and bio synthesis gas have been emerged as important platform chemicals for the production of fine chemicals and sustainable fuels.

Furan derivatives, such as 5-hydroxymethyl-2-furaldehyde (HMF) derived from renewable biomass resource, has the potential to be served as substitutes for the petroleum-based building blocks which are currently used in the production of polymers and fine chemicals. In Section 1 (Chapter 1), reduced graphene oxide (RGO) is one of the most promising catalyst supports since its faintly acidic sites together with large amount of functional groups on its surface. In this section, it has been proved that, and for the first time, Pt loaded RGO (Pt/RGO) is an efficient, robust and durable catalyst oxidizing 5-hydroxymethylfufural (HMF) to 2,5-furandicarboxylic acid (FDCA) directly under mild conditions. The selectivity of FDCA is up to 84% along with 100% HMF conversion in the presence of excess base. We deduce that the total reaction on Pt/RGO catalyst includes several consecutive steps, in which 5-hydroxymethyl-2-furancarboxylic acid (HMFCA) acts as an intermediate. The finding in this section is a significant advance not only for RGO-based catalysts development, but also for FDCA scalable production, because the total reaction is performed smoothly without using previously reported harsh reaction conditions.

Furthermore, Cellulose, which is a polysaccharide mainly composed of glucose via β-1-4 glycosidic linkage, exists widely in biomass resources. The utilization of cellulose is usually achieved through two steps: being hydrolyzed selectively into glucose and

further converted into chemicals and fuels. The sugar alcohols, especially sorbitol, are not only used as sweetener in diet foods, but also as an important basic chemical for the production of sustainable chemicals and fuels. In Section 2 (chapter 2-5), Pt nanocatalysts loaded on reduced graphene oxide (Pt/RGO) are prepared using a convenient microwave-assisted reduction approach with ethylene glycol as reductant. The conversion of cellulose or cellobiose into sorbitol is used as application reaction to investigate their catalytic performance. Various metal nanocatalysts loaded on RGO are compared. Pt/RGO exhibits the highest catalytic activity with 91.5% of sorbitol yield from cellobiose. The catalytic performances are compared with Pt nanocatalysts supported on different carbon materials or on silica support. The result shows that RGO is the best catalyst support, and the yield of sorbitol is as high as 91.5% from cellobiose and 58.9% from cellulose, respectively. The improvement of catalytic activity is attributed to the appropriate Pt particle size and hydrogen spillover effect of Pt/RGO catalyst. Interestingly, the size and dispersion of supported Pt particle are easily regulated by convenient adjustment of the microwave heating temperature. The catalytic performance is found increased firstly and then decreased with the particle size increased. The optimum Pt particle size is 3.6 nm. These results may offer useful guidelines to design novel catalysts with beneficial catalytic performance for biomass conversion.

Conversion of synthesis gas (a mixture of CO and H_2), which is derived from biomass, is a hot field in hydrocarbon production. Fischer-Tropsch synthesis is a set of catalytic processes that can be used to produce chemicals and fuels from synthesis gas. Combining a acidic zeolite with common FTS catalyst can produce isoparaffins for

gasoline-ranged component. Tuning hydrocarbons distribution in Fischer-Tropsch synthesis is greatly challenging in Section 3 (chapter 6) by employing three different pathways to deposit trace Palladium on Co/H-ZSM5 catalyst, tunable isoparaffin and olefin selectivity is achieved successfully. The impregnated Pd shows a poor promotion of Co dispersion and reducibility, producing a slight enhancement of FTS activity and isoparaffin selectivity. Pd sputtering induces a re-dispersion of impregnated Co/H-ZSM5 particles and Pd is deposited with an intimate distance to Co species and with a weak interaction combining zeolite, due to which complete hydrogenation of olefins is achieved. But the surface enriched Pd on pre-sputtered Co catalyst was can form Pd-Co nano-alloys, suppressing the chain growth activity by excessive hydrogenation process.

Reference

1 Y. Roman-Leshkov, C. J. Barret, Z. Y. Liu, J. A. Dumesic, *Nature*, 2007, **447**, 982.

2 T. El Hajj, A. Masroua, J. C. Martin, G. Descotes, *Bull. Soc. Chim. Fr.*, 1987, **5**, 855.

3 Y. Su, H. M. Brown, X. Huang, X. Zhou. J. E. Amonette, Z. C. Zhang, *Appl. Catal. A*, 2009, **361**,117.

4 A. Gandini, M. N. Belgacem, *Prog. Polym. Sci.*, 1997, **22**, 1203.

5 Top value Added Chemicals from Biomass, US department of Energy report, August 2004, ed. T. Werpy, G. Petoser.

6 T. Miura, H. Kakinuma, T. Kawano, H. Matsuhisa, U.S Patent, US-7411078, 2008.

7 W. Partenheimer, V. V. Grushin, *Adv. Synth. Catal.*, 2001, **343**, 102.

8 P. Vinke, W. Van der Poel, H. Van Bekkum, *Stud. Surf. Sci. Catal*., 1991, **59**, 385.

9 M. Kroger, U. Prusse, K. D. Vorlop, *Top Catal.*, 2002, **13**, 237.

10 B. W. Lew (Atals Chemistry Industries, Inc.) U.S Patent, US-3326994, 1967.

11 E. I. Leupold, M. Wiesner, M. Schilingmann, K. Kapp, (Hoechst AG) Eur. Patent Ep 0356703, 1993.

12 M. A. Lilga, R. T. Hallen, M. Gray, *Top Catal.*, 2010, **53**, 1264.

13 S. E. Davis, N. B. Zope, R. J. Davis, *Green Chemistry*, 2012,**14**, 143.

14 N. K. Gupta, S. Nishimura, A. Takagaki, K. Ebitani, *Green Chemistry*, 2011, **13**, 824.

15 K. R. Vuyyuru, P. Strasser, *Catal. Today*, 2012, **195**, 144.

16 P. Verdeguer, N. Merat, A. Gaset, *J. Mol. Catal.*, 1993, **85**, 327.

17 S. E. Davis, L. R. Houk, E. C. Tamargo, A. K. Datye, R. J. Davis, *Catal. Today*, 2011,**160**, 55.

18 G. Shi, C. Huang, C. Li, *Energy. Eviron. Sci.*, 2012, **5**, 8848.

19 X. Chu, Q. Zhu, W. L. Dai, K. Fan, *RSC Adv.*, 2012, **2**, 7135.

20 A. Dhakshinamoorthy, M. Alvaro, P. Concepcion, V. Fornes, H. Gracia, *Chem. Commun.*, 2012, **48**, 5443.

21 D. R. Dreyer, H. P. Jia, C. W. Bielawski, *Angew. Chem. Int. Ed.*, 2010, **49**, 6813.

22 S. Wu, Q. He, C. Zhou, X. Qi, X. Huang, Z. Yin, Y. Yang, H. Zhang, *Nanoscale,* 2012, **4**, 2478.

23 W. S. Hummers Jr, R. E. Offeman, *J. Am. Chem. Soc.*, 1958, **80**, 1339.

24 A. Bonanni, A. Ambrosi, C. K. Chua, M. Pumera, *ACS Nano,* 2014, **8**, 4197.

25 A. F. Faria, D. S. T. Martinez, A. C. M. Moraes, M. E. H. M. Costa, E. B. Barros, A. G. S. Filho, A. J. Paula, O. L. Alves, *Chem. Mater.*, 2012, **24**, 4080.

26 J. P. Rourke, P. A. Pandey, J. J. Moore, M. Bates, I. A. Kinloch, R. J. Young, N. R. Wilson, *Angew. Chem. Int. Ed.*, 2011, **50**, 3173.

27 A. M. Ruppert, K. Weinberg, R. Palkovits, *Angew. Chem. Int. Ed.* 2012**, 51**, 2564.

28 M. S. Mettler, S. H. Mushrif, A. D. Paulsen, A. D. Javadekar, D. G. Vlachos, P. J. Dauenhauer, *Energy Environ. Sci.* 2012**, 5**, 5414.

29 K. Kohse-Höinghaus, P. Oßwald, T. A. Cool, T. Kasper, N. Hansen, F. Qi, C. K. Westbrook, P. R. Westmoreland, *Angew. Chem. Int. Ed.* 2010**, 49**, 3545.

30 H. Kobayashi, H. Ohta, A. Fukuoka, *Catal. Sci. Technol.* 2012**, 2**, 869.

31 C. Luo, S. Wang, H. Liu, *Angew. Chem. Int. Ed.* 2007**, 46**, 7636.

32 D. An, A. Ye, W. Deng, Q. Zhang, Y. Wang, *Chem. Eur. J.* 2012**, 18**, 2938.

33 N. Ji, T. Zhang, M. Zheng, A. Wang, H. Wang, X. Wang, J. G. Chen, *Angew. Chem. Int. Ed.* 2008**, 120**, 8638.

34 L. N. Ding, A. Q. Wang, M. Y. Zheng, T. Zhang, *ChemSusChem* 2010**, 3**, 818.

35 A. Fukuoka, P. L. Dhepe, *Angew. Chem. Int. Ed.* 2006**, 45**, 5161.

36 H. Wang, L. Zhu, S. Peng, F. Peng, H. Yu, J. Yang, *Renew. Energ.* 2012**, 37**, 192.

37 P. Yang, H. Kobayashi, K. Hara, A. Fukuoka, *ChemSusChem* 2012**, 5**, 920.

38 S. You, I. Baek, Y. Kim, K.-E. Jeong, H.-J. Chae, T.-W. Kim, C.-U. Kim, S.-Y. Jeong, T. Kim, Y.-M. Chung, S.-H. Oh, E. Park Korean, *J. Chem. Eng.* 2011**, 28**, 744.

39 J. Pang, A. Wang, M. Zheng, Y. Zhang, Y. Huang, X. Chen, T. Zhang, *Green Chem.* 2012**, 14**, 614.

40 C. Huang, C. Li, G. Shi, *Energy Environ. Sci.* 2012**, 5,** 8848.

41 X. Chu, Q. Zhu, W.-L. Dai, K. Fan, *RSC Advances* 2012**, 2**, 7135.

42 A. Dhakshinamoorthy, M. Alvaro, P. Concepcion, V. Fornes, H. Garcia, *Chem. Commun.* 2012**, 48**, 5443.

43 D. R. Dreyer, H.-P. Jia, C. W. Bielawski, *Angew. Chem. Int. Ed.* 2010**, 49**, 6813.

44 J. Zhu, Y. K. Sharma, Z. Zeng, X. Zhang, M. Srinivasan, S. Mhaisalkar, H. Zhang, H. H. Hng, Q. Yan, *J. Phys. Chem. C.* 2011**, 115**, 8400.

45 Z. Sun, X. Lu, *Ind. Eng. Chem. Res.* 2012**, 51**, 9973.

46 J. Wang, T. Tsuzuki, B. Tang, X. Hou, L. Sun, X. Wang, *ACS Appl. Mat. Interfaces* 2012**, 4**, 3084.

47 M.-S. Wu, Y.-P. Lin, C.-H. Lin, J.-T. Lee, *J. Mater. Chem.* 2012**, 22**, 2442.

48 S. Wu, Q. He, C. Zhou, X. Qi, X. Huang, Z. Yin, Y. Yang, H. Zhang, *Nanoscale* 2012**, 4**, 2478.

49 Y. Li, W. Gao, L. Ci, C. Wang, P. M. Ajayan, *Carbon* 2010**, 48**, 1124.

50 N. Yan, C. Zhao, C. Luo, P. J. Dyson, H. Liu, Y. Kou, *J. Am. Chem. Soc.* 2006**, 128**, 8714.

51 W. S. Hummers, R. E. Offeman, *J. Am. Chem. Soc.* 1958**, 80**, 1339.

52 A. Kaniyoor, T. T. Baby, S. Ramaprabhu, *J. Mater. Chem.* 2010**, 20**, 8467.

53 D. Wang, G. Yang, Q. Ma, M. Wu, Y. Tan, Y. Yoneyama, N. Tsubaki, *ACS Catal.* 2012**, 2**, 1958.

54 J. Li, H. Lin, Z. Yang, J. Li, *Carbon* 2011**, 49**, 3024.

55 Y. Guo, C. Bao, L. Song, B. Yuan, Y. Hu, *Ind. Eng. Chem. Res.* 2011**, 50**, 7772.

56 V Jollet, F. Chambon, F. Rataboul, A. Cabiac, C. Pinel, E. Guillon, N. Essayem, *Green Chem.* 2009**, 11**, 2052.

57 W Deng, R Lobo, W Setthapun, ST Christensen, J. W. Elam. C. L. Marshall, *Catal. Lett.* 2011**, 141**, 498.

58 X. Huang, X. Qi, F. Boey, H. Zhang, *Chem. Soc. Rev.* 2012, **41**, 666.

59 Y. B. Huang, Y. Fu, *Green Chem*. 2013**, 15**, 1095.

60 Y. J. Gao, D. Ma, C. L. Wang, J. Guan, X. H. Bao, *Chem. Commun.* 2011**, 47**, 2432.

61 M. Baghbanzadeh, L. Carbone, P. D. Cozzoli, C. O. Kappe, *Angew. Chem. Int. Ed.* 2011**, 50**, 2.

62 C. O. Kappe, *Chem. Soc. Rev.* 2008**, 37**, 1127.

63 X. Huang, X. Qi, F. Boey, H. Zhang, *Chem. Soc. Rev.* 2012, **41**, 666.

64 R. S. Oosthuizen, V. O. Nyamori, Platinum Metals Rev., 2011, **55**, 154.

65 S. Barrientos-Ramírez, G. Montes de Oca-Ramírez, A. Sepúlveda-Escribano, M.M. Pastor-Blas, A. González-Montiel, F. Rodríguez-Reinoso, Catal. Today 2010, **150**, 42.

66 D. Vervloet, F. Kapteijn, J. Nijenhuis and J. R. van Ommen, *Catal. Sci. Technol.*, 2012, **2**, 1221.

67 B. Sun, G. Yu, J. Lin, K. Xu, Y. Pei, S. Yan, M. Qiao, K. Fan, X. Zhang and B. Zong, *Catal. Sci. Technol.*, 2012, **2**, 1625.

68 J. Sun, C. Xing, H. Xu, F. Meng, Y. Yoneyama and N. Tsubaki, *J. Mater. Chem. A*, 2013, **1**, 5670.

69 W. D. Shafer, G. Jacobs and B. H. Davis, *ACS Catal.*, 2012, **2**, 1452-1456.

70 S. Sartipi, K. Parashar, M. Makkee, J. Gascon and F. Kapteijn, *Catal. Sci. Technol.*, 2013, **3**, 572.

71 N. Tsubaki, Y. Yoneyama, K. Michiki and K. Fujimoto, *Catal. Commun.*, 2003, **4**, 108.

72 S. Sartipi, K. Parashar, M. J. Valero-Romero, V. P. Santos, B. van der Linden, M. Makkee, F. Kapteijn and J. Gascon, *J. Catal.*, 2013, **305**, 179.

73 W. P. Ma, G. Jacobs, R. A. Keogh, D. B. Bukur and B. H. Davis, *Appl. Catal. A*, 2012, **437**, 1.

74 H. Karaca, O. V. Safonova, S. Chambrey, P. Fongarland, P. Roussel, A. Griboval-Constant, M. Lacroix and A. Y. Khodakov, *J. Catal.*, 2011, **277**, 14.

75 N. Tsubaki, S. Sun and K. Fujimoto, *J. Catal.*, 2001, **199**, 236.

76 M. Minnermann, S. Pokhrel, K. Thiel, R. Henkel, J. Birkenstock, T. Laurus, A. Zargham, J. I. Flege, V. Zielasek, E. Piskorska-Hommel, J. Falta, L. Madler and M. Baumer, *J. Phys. Chem. C*, 2011, **115**, 1302.

77 T. Abe, M. Tanizawa, K. Watanabe and A. Taguchi, *Energy Environ. Sci.*, 2009, **2**, 315.

78 J. Sun, X. Li, A. Taguchi, T. Abe, W. Niu, P. Lu, Y. Yoneyama and N. Tsubaki, *ACS Catal.*, 2014, **4**, 1.

79 X.-G. Li, C. Liu, J. Sun, H. Xian, Y.-S. Tan, Z. Jiang, A. Taguchi, M. Inoue, Y. Yoneyama, T. Abe and N. Tsubaki, *Sci. Rep.*, 2013, **3**, 2813.

80 J. He, Z. Liu, Y. Yoneyama, N. Nishiyama and N. Tsubaki, *Chem. Eur. J.*, 2006, **12**,

8296.

81 M. Inoue, H. Shingen, T. Kitami, S. Akamaru, A. Taguchi, Y. Kawamoto, A. Tada, K. Ohtawa, K. Ohba, M. Matsuyama, K. Watanabe, I. Tsubone and T. Abe, *J. Phys. Chem. C*, 2008, **112**, 1479.

82 S. Zafeiratos, F. Paloukis, G. Papakonstantinou, D. Teschner, M. Hävecker, E. Vass, P. Schnörch, A. Knop-Gericke, R. Schlögl and B. Moreno, *Catal. Today*, 2010, **157**, 250.

83 A. F. Carlsson, M. Naschitzki, M. Bäumer and H. J. Freund, *J. Phys. Chem. B*, 2002, **107**, 778.

84 C. Evangelisti, N. Panziera, P. Pertici, G. Vitulli, P. Salvadori, C. Battocchio and G. Polzonetti, *J. Catal.*, 2009, **262**, 287.

85 M. Krawczyk and J. W. Sobczak, *Appl. Surf. Sci.*, 2004, **235**, 49.

86 A. Martínez-Hernández and G. A. Fuentes, *Appl. Catal. B*, 2005, **57**, 167.

87 P. Sangeetha, K. Shanthi, K. S. R. Rao, B. Viswanathan and P. Selvam, *Appl. Catal. A*, 2009, **353**, 160.

88 K. Cheng, J. Kang, S. Huang, Z. You, Q. Zhang, J. Ding, W. Hua, Y. Lou, W. Deng and Y. Wang, *ACS Catal.*, 2012, **2**, 441.

Acknowledgements

I would like to acknowledge Professor Noritatsu Tsubaki, my academic advisor, for his invaluable guidance, innovative suggestions, continued patience and support during my doctoral course in University of Toyama. He is always in pursuit of excellence, and he left an inspiration to me. I am also very grateful to Professor Yoshiharu Yoneyama for his scientific advice and knowledge and many insightful discussions and suggestions. I will forever be thankful to my former college research advisor in Department of Pharmaceutical Science, Professor Takayuki Yakura for giving me the opportunity to be the Japan Government scholarship candidate in 2009.

I am extreme grateful to Dr. Guohui Yang and Dr. Jian Sun in Tsubaki group. They have been helpful in providing advice many times during my doctoral course career. I thank all the members of the Tsubaki group, expecially Dr. Ding Wang, Dr. Yuzhou Jin, Dr. Peng Lu and Dr. Minghui Tan, Dr. Qinhong Wei, Mr. Masahiro Kyodo, Mr. Atsushi Shimoharai, Mr. Nobiyoshi Muranaka for their deep friendship and lots of helpful advice.

Here, I have to express my respect to Professor Maosheng Cheng in Shenyang Pharmaceutical University, P.R.China. I started my research career under his guidance in Department of Medicinal Chemistry.

Finally, and most importantly, I would like to thank my dad and my mom for their love. Their support, encouragement, quiet patience and unwavering love were

undeniably the bedrock upon which the past 27 years of my life have been built.

Publication List

1. "Pt Nanoparticles Loaded on Reduced Graphene Oxide as an Effective Catalyst for the Direct Oxidation of 5-Hydroxymethylfufural (HMF) to Produce 2,5-Furandicarboxylic Acid (FDCA) under Mild Conditions"
Wenqi Niu, Ding Wang, Guohui Yang, Jian Sun, Mingbo Wu, Yoshiharu Yoneyama, Noritatsu Tsubaki
Bull. Chem. Soc. Jpn. 2014, **87**, 1124-1129.

2. "Pt Nanocatalysts Supported on Reduced Graphene Oxide for Selective Conversion of Cellulose or Cellobiose to Sorbitol"
Ding Wang, **Wenqi Niu**, Mingbo Wu, Minghui Tan, Xuejun Zheng, Yanpeng Li, Noritatsu Tsubaki
ChemSusChem., 2014, **7**, 1398-1406.

3. "Combining Wet Impregnation and Dry Sputtering to Prepare Highly-Active CoPd/H-ZSM5 Ternary Catalysts Applied for Tandem Catalytic Synthesis of Isoparaffins"
Jian Sun, **Wenqi Niu**, Akira Taniguchi, Takayuki Abe, Yoshiharu Yoneyama, Noritatsu Tsubaki.
Catal. Sci. Technol., *2014*, **4**, 126

4. "Synthesis of dipropyl carbonate over calcined hydrotalcite-like compounds containing La"
Qingxiang Ma, Tiansheng Zhao, Ding Wang, **Wenqi Niu**, Peng Lv, Noritatsu Tsubaki.
Applied Catalysis A,Vol. 464-465, 142-148, 2013

5. "Highly-Dispersed Metallic Ru Nanoparticles Sputtered on H-Beta Zeolite for Directly Converting Syngas to Middle iso-Paraffins"
Jian Sun, X. Li, Akira Taguchi, Takayuki Abe, **Wenqi Niu**, Peng Lu, Yoshiharu Yoneyama, Noritatsu Tsubaki.
ACS Catalysis, 4, 1-8, 2014